



Contribution of the wind, Loop Current Eddies, and topography to the circulation in the southern Gulf of Mexico

Erick R. Olvera-Prado¹ · Rosario Romero-Centeno¹ · Jorge Zavala-Hidalgo¹ · Efraín Moreles² · Angel Ruiz-Angulo³

Received: 5 May 2022 / Accepted: 1 August 2023 / Published online: 29 September 2023
© The Author(s) 2023

Abstract

The Bay of Campeche, located in the southern Gulf of Mexico (GoM), is characterized by a semi-permanent cyclonic circulation commonly referred to as the Campeche Gyre (CG). Several studies documenting its upper layer structure have suggested a possible relationship between its seasonal variability and the wind stress, and that non-seasonal variability arises mainly from the interaction of the gyre with Loop Current Eddies (LCEs) that arrive in the region. Nevertheless, a partition of the contributions of these forcings to the circulation of the CG in a statistically consistent manner is still needed. This study examines the wind- and eddy-driven circulation with long-term numerical simulations of the GoM using the HYbrid Coordinate Ocean Model. Our results show that, in the absence of LCEs, the wind can sustain a seasonal-modulated circulation in the CG, confined within the upper 600 m. When considering LCEs, high fluctuations on the flow at intraseasonal time scales are imposed. We found that the LCEs influence the western Bay of Campeche circulation through two main mechanisms: (a) by decelerating and inhibiting the CG through a positive vorticity flux out of the bay, leading to reversals in the flow if LCE southward penetration is large, or (b) by strengthening the CG when a big cyclone, accompanying the LCE, enters the region. It is proposed that the second mechanism is responsible for inducing a net weak cyclonic circulation in the Bay in the absence of wind. Furthermore, past studies have shown that the CG behaves as an equivalent-barotropic flow, with topography acting to confine the CG to the west of the bay. In our modeling results, the role of topography manifests similarly among the different numerical experiments, resulting in closed geostrophic contours to the west of the bay that confine an upper-layer, nearly-symmetric, equivalent-barotropic CG.

Keywords Gulf of Mexico · Campeche Gyre · Seasonal variability · Non-seasonal variability · Topographic control · HYCOM

1 Introduction

The Bay of Campeche (BoC) is a semi-enclosed region located in the southern Gulf of Mexico (GoM), bound to the west, south, and east by the coast of Mexico and connected with GoM waters to the north. Its bathymetry follows approximately a U shape with a smooth slope on the western side and a rough slope to the east. The western part of the BoC is characterized by a semi-permanent cyclonic circulation, often referred to as the Campeche Gyre (CG) (Monreal-Gómez and Salas de León 1997), in waters of depths greater than 1000 m,

while the circulation on the shelves presents strong seasonality driven by the wind (Zavala-Hidalgo et al. 2003). Several observational, theoretical, and numerical studies have documented the surface and vertical extension of the CG; nevertheless, the role of the processes responsible for sustaining the CG, and their relative contribution to its seasonal and non-seasonal variability, are still not fully understood. These processes are the wind stress curl (Gutiérrez de Velasco and Winant 1996; Vázquez et al. 2005; Dimarco et al. 2005), eddy-driven vorticity fluxes (Ohlmann et al. 2001; Vidal et al. 1992), and the confinement effect of the topography (Pérez-Brunius et al. 2013; Zavala Sansón 2019).

Using a set of observational data, Vázquez et al. (2005) presented the first evidence that the observed long-term mean cyclonic circulation within the BoC (in the upper 800 m) could be forced by the positive wind stress curl that prevails in the region (Gutiérrez de Velasco and Winant 1996)

Responsible Editor: Ricardo de Camargo

✉ Erick R. Olvera-Prado
erick@atmosfera.unam.mx

Extended author information available on the last page of the article

via Sverdrup dynamics, inferring the existence of a western boundary current at 20° N that balances the northward transport within the BoC caused by the wind. From their near-surface drifter analysis, a winter maximum and summer minimum were found in the western boundary current; however, the authors considered that the drifter records were not sufficiently long to establish the seasonal variability of the mean circulation in a statistically reliable manner. Furthermore, they found that the geostrophic transport estimated from the hydrographic data is in agreement with the Sverdrup transport estimated from the mean wind stress curl (~ 4 Sv). Pérez-Brunius et al. (2013) found no significant differences in mean currents between winter and summer from high-resolution mooring and drifter data, although the mean values suggest a slight intensification at the western boundary during winter. However, they consider that there is still no conclusive evidence of a western intensified flow in any of the seasons.

Previous research indicates that Loop Current Eddies (LCEs) traveling on a southern path (Vukovich 2007) towards the western boundary and colliding with it influence the CG variability. Ohlmann et al. (2001) showed that mesoscale eddies play a role as important as wind stress in driving the overall GoM circulation on long time scales. Vidal et al. (1992) concluded that the collision of a LCE with the southwestern continental shelf led to a transfer of mass and angular momentum towards the south, thus producing a cyclonic gyre in the BoC. In their numerical study, Romanou (2004) suggested that the cyclonic circulation in the BoC is caused by accretion of cyclones generated in the western Gulf by interaction of LCEs with the continental slope. From an empirical orthogonal function analysis of 8 years of altimetry data, Vázquez et al. (2005) found evidence of a net eddy flux into the BoC which manifests as smaller-in-size cyclones and anticyclones entering the region, which they hypothesized are generated when LCEs collide with the western continental slope. However, they state that while such eddy flux can explain the non-seasonal character of the circulation, this is simply a supplement superimposed on a larger-scale permanent cyclonic circulation due to the wind stress curl over the BoC. More recently, with the aid of 3 years of surface drifters and altimetry data, Pérez-Brunius et al. (2013) analyzed three examples of LCEs influencing the CG circulation. The authors found no clear evidence of an influx of positive vorticity into the BoC by cyclones generated by LCE collisions with the western boundary. In fact, in two of the three cases analyzed, they found that the presence of LCEs at the northwestern boundary nearly disrupted the cyclonic gyre rather than intensifying it, draining it of its waters while pushing it towards the southwestern shelf.

Pérez-Brunius et al. (2013) addressed the confinement effect of the bathymetry on the CG with 3 years of current meter moorings. The authors evaluated the vertical

coherence of the flow and found that the cyclonic gyre is vertically coherent and nearly unidirectional, consistent with an equivalent-barotropic flow with an equivalent depth of $H_0 = 650\text{m}$. This results in closed geostrophic contours in the western BoC, explaining, by potential vorticity conservation, the location and symmetry of the CG west of 94° W. Zavala Sansón (2019) studied the formation of the CG with a nonlinear, time-dependent, equivalent-barotropic model. The author performed idealized wind-driven simulations with decremental values of the reference depth and found that, when $H_0 = 650\text{m}$, the resemblance of the cyclonic gyre with the CG is high, confirming that the positive circulation over the BoC is compatible with equivalent-barotropic dynamics.

In this study, we address the contribution of the wind and LCEs to the mean, seasonal, and intraseasonal variability of the circulation in the western BoC. What distinguishes this study is that we use a set of long-term, free-running simulations conducted with an ocean general circulation model with realistic bathymetry and stratification structure, isolating the effects of these processes to discern their relative contributions. First, the separate and joint mean effect of wind and LCEs on the extent and vertical structure of the CG is examined, providing insights into the role of topography under these different dynamic conditions. We also explored the role of the wind stress curl in modulating the seasonal variability of the CG in the presence and absence of LCEs. Finally, we discuss the non-seasonal variability of the CG induced by LCEs entering the northern BoC and examine the associated vorticity flux. Our results contribute to a better understanding of the effect of these forcings on the circulation of the BoC in a statistically consistent manner and thus advance in the understanding of the dynamics of the region. The model configuration, validation, and analysis methods used are described in Section 2; results and discussion, including the analysis of the mean state and vertical structure of the CG, and its seasonal and non-seasonal modulation, are presented in Section 3. A brief concluding summary is provided in Section 4.

2 Model and methods

2.1 The numerical simulations

To address the contribution of the different processes to the circulation in the BoC, three free-running simulations of the GoM with incremental complexity and realism were conducted employing the HYbrid Coordinate Ocean Model (HYCOM). HYCOM uses a generalized hybrid vertical coordinate system that allows vertical coordinates to follow isopycnal layers in the deep stratified ocean and transition to pressure coordinates or terrain-following coordinates in unstratified regions or coastal areas, respectively (Bleck

Table 1 Specifications of the numerical simulations using the HYCOM model. OBW is the control run, NoOBW corresponds to the experiment with closed boundary conditions, and OBNoW corresponds to the experiment without atmospheric forcing

| Experiment | OBW (control) | NoOBW | OBNoW |
|-----------------------------------|--|-----------------------|-----------------------|
| Hycom version | 2.3.01 | 2.3.01 | 2.3.01 |
| Lateral boundaries | Monthly climatology | No | Monthly climatology |
| Atmospheric forcing | Hourly (CFSR) | Hourly (CFSR) | No |
| Vertical coordinates | 36 hybrid layers | 36 hybrid layers | 36 hybrid layers |
| Initialization | (1-Jan-1994) | Hotstart (1-Jan-1995) | Hotstart (1-Jan-1995) |
| Length (years) | 19 | 19 | 19 |
| Baroclinic time step | 120 s | 120 s | 120 s |
| Barotropic time step | 7.5 s | 7.5 s | 7.5 s |
| Reference density (σ) | 34 | 34 | 34 |
| Vertical turbulence | KPP | None | KPP |
| Sea surface salinity nudging | Generalized Digital and Environmental Model-V4.0 | | |
| Sea surface temperature nudging | Generalized Digital and Environmental Model-V4.0 | | |
| Quadratic bottom drag coefficient | Spatially varying (min = 2.49×10^{-3} , max = 7.54×10^{-3}) | | |
| Velocity diffusion (velfd2) (m/s) | Spatially varying (min = 2.36×10^{-3} , max = 2.65×10^{-3}) | | |
| Horizontal viscosity | Max[background Laplacian (velfd2), Smagorinsky] + biharmonic (0.02 m/s) | | |

2002; Chassignet et al. 2006). The horizontal domain covers the GoM, the northwestern Caribbean Sea, and part of the western North Atlantic Ocean ($(98^\circ \text{W}, 77^\circ \text{W}) \times (18^\circ \text{N}, 32^\circ \text{N})$) (Fig. 1a), with a spatial resolution of $1/25^\circ$ ($\sim 3.8\text{--}4.2$ km) and 36 hybrid vertical layers, which are mainly isopycnal layers in the open ocean below the mixed layer and z-layers above it. The model bathymetry is an integration from different sources: the one from the HYCOM website (hycom.org), the General Bathymetric Chart of the Oceans, and corrected data from different sources, mainly observations collected during several cruises. Monthly climatology of river inflow is included at 40 locations along the coast, and no data assimilation nor tidal forcing was used. Complete details of the model parameters for the three experiments are listed in Table 1.

The three simulations share the specifications mentioned above. The experiment OBW (open boundaries with wind) is the control run since it is the most realistic simulation; in experiment NoOBW (no open boundaries with wind), the lateral boundaries are closed to remove the Loop Current system and thus the influence of LCEs and focus on the isolated effect of wind over the BoC; and in experiment OBNoW (open boundaries without wind), the atmospheric forcing is turned off in order to discern the influence of LCEs in the absence of wind forcing. OBW is initialized from the mean state of January, 1994 of the $1/12^\circ$ GOFS 3.1 HYCOM global reanalysis (GLBb0.08-53.X) (Metzger et al. 2017), reaching statistical stability within a few months (as can be seen in the time series of global mean kinetic energy averaged over the 3D domain in Fig. 3g red line). Then, NoOBW and OBNoW

were initialized from a 1-year spin-up of the OBW output (January 1st, 1995). After statistical stability is reached in these experiments (see Fig. 3g blue and green lines), they were integrated from 1997 to 2015, which encompasses the analysis period for this study.

OBW and OBNoW were nested in the global reanalysis using monthly boundary conditions from a 22-year climatology (1994–2015) (<ftp://ftp.hycom.org/pub/GitHub/HYCOM-examples/GOMb0.08/datasets/subregion.tar.gz>). This monthly climatology is repeated each year to produce the continuous 19-year model integration; therefore, no interannual variability is imposed at the lateral open boundaries. Following spin-up, hourly atmospheric forcing (10-m wind speed, 2-m air temperature, 2-m atmospheric humidity, surface shortwave and longwave heat fluxes, surface atmospheric pressure, and precipitation) is prescribed for OBW and NoOBW using the Climate Forecast System Reanalysis (CFSR) Saha et al. 2010) from 1997 to 2015. Wind stress is calculated using bulk formulas during model run time taking into account the surface ocean current speed. The target densities, which define the vertical grid in the model, are inherited from the global reanalysis. The outputs of the model, which include the estimated wind stress fields, were recorded every day.

2.2 Validation of the model

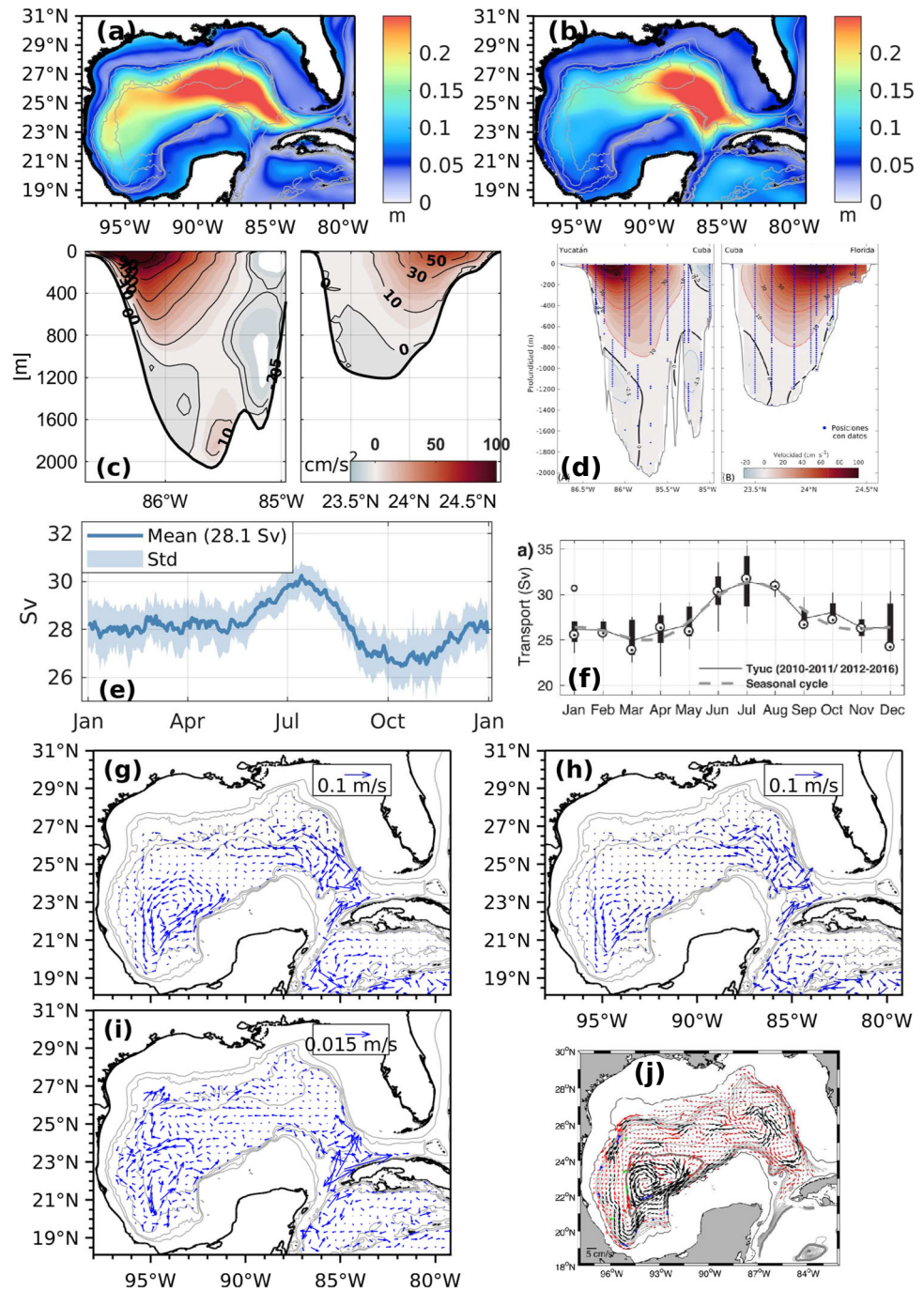
The evaluation of the model performance consisted in verifying that the major characteristics of the GoM circulation were in statistical agreement to those obtained based on

observations; this provides confidence that the CG and its response to the LCEs and wind forcings are realistic. The validation is carried out on the OBW experiment (control). Here, we compare statistical analysis derived from simulated velocity and sea surface height (SSH) with analysis of in situ and remote sensing observations. Some of the diagnostics presented here follow the methodology used in Morey et al. (2020). In general, the simulation is able to reproduce the more energetic patterns and the intrinsic variability of the GoM, including its amplitude, location, and evolution.

2.2.1 Mean circulation and transport

Figure 1a shows the standard deviation of SSH anomalies from the OBW experiment and Fig. 1b that computed with the Copernicus Marine Environment Monitoring Service (CMEMS) database (<https://doi.org/10.48670/moi-00148>). CMEMS consists of daily instantaneous maps of SSH anomalies in a $0.25^\circ \times 0.25^\circ$ grid and covers the period from January 1st, 1993, to December 31st, 2020. The model produces a relatively realistic variability, with a primary area of

Fig. 1 Model validation: standard deviation of the SSH anomalies from **a** OBW and **b** CMEMS (<https://doi.org/10.48670/moi-00148>); mean along-channel velocity component in the Yucatan Channel and Florida Straits from **c** OBW and **d** mooring data (from Candela et al. (2019)); climatological transport through the Yucatan Channel from **e** OBW and **f** mooring data (from Athie et al. (2020)); and mean deep circulation between 1500 and 2500 m for experiments **g** OBW, **h** OBNoW, **i** NoOBW, and from **j** observations (from Pérez-Brunius et al. (2018))



high values within the LC extension and retraction region and a secondary area highlighting the preferred paths of the LCEs and the otherwise known LCE graveyard, while CMEMS depicts smaller values in the western GoM. In the BoC, small standard deviation values are found in both datasets, indicating persistence of the flow. The structure of the mean along-channel velocity through the Yucatan Channel and the Florida Straits for the 19 years of simulation is shown in Fig. 1c and from observations in Fig. 1d. Observations come from in situ moorings deployed during the CANEK project (Candela et al. 2019) and cover the period from July 2012 to July 2018. In general, the model is consistent with obser-

vations; the Yucatan main current and counter-current are overall well represented, with the core of the main current placed at $\sim 86.3^\circ W$. The core of the current in the Florida Straits is $\sim 40\text{ cm/s}$ weaker ($\sim 100\%$) and depicts a northern displacement ($\sim 0.15^\circ$) in the model compared to observations. The modeled Yucatan Channel climatological transport shows strong seasonality (Fig. 1e), with a mean of about 28 Sv, which is within the range of published estimates ranging from 23.8 to 30.3 Sv (Athié et al. 2015; Rousset and Beal 2010; Sheinbaum et al. 2002). The model exhibits moderate interannual variability in the transport, which is to be expected given that there is no interannual variability at the

Table 2 Characteristics of the LCE separation events from the OBW experiment: 1 January 1997 through 31 December 2015

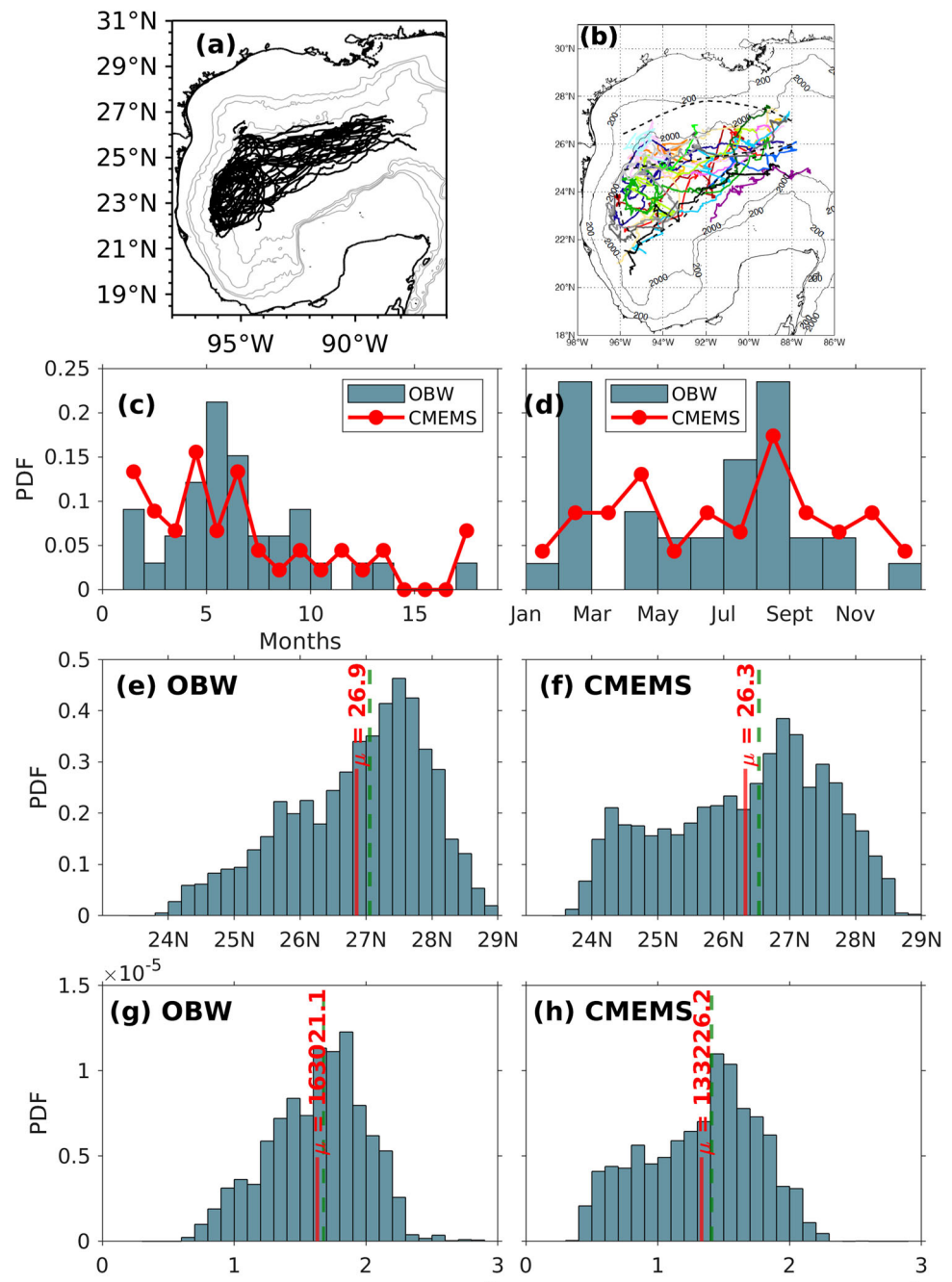
| LCE number | Separation date | Separation period (months) | Lifespan (days) | Reached BoC | Area (km ²) |
|------------|-----------------|----------------------------|-----------------|-------------|-------------------------|
| 1 | 28 Aug 1997 | 15.03 | 385 | Yes | 68,345 |
| 2 | 20 May 1998 | 8.72 | 345 | Yes | 62,309 |
| 3 | 7 Oct 1998 | 4.61 | 325 | No | 22,877 |
| 4 | 19 Jul 1999 | 9.37 | 249 | No | 38,591 |
| 5 | 26 Oct 1999 | 3.26 | 323 | Yes | 34,181 |
| 6 | 26 May 2000 | 7.2 | 154 | No | 28,849 |
| 7 | 21 Jul 2000 | 1.84 | 377 | Yes | 94,699 |
| 8 | 22 Feb 2001 | 7.11 | 288 | Yes | 32,760 |
| 9 | 18 Aug 2001 | 5.82 | 367 | Yes | 55,429 |
| 10 | 27 Feb 2002 | 6.35 | 285 | Yes | 46,921 |
| 11 | 30 Aug 2002 | 6.05 | 254 | No | 37,098 |
| 12 | 26 Feb 2003 | 5.92 | 315 | Yes | 48,936 |
| 13 | 17 Aug 2003 | 5.66 | 394 | Yes | 72,537 |
| 14 | 7 Apr 2004 | 7.7 | 268 | No | 44,799 |
| 15 | 23 Feb 2005 | 10.59 | 295 | Yes | 64,517 |
| 16 | 19 Aug 2005 | 5.82 | 355 | Yes | 67,259 |
| 17 | 5 Feb 2006 | 5.59 | 392 | No | 33,606 |
| 18 | 12 Jul 2007 | 17.17 | 426 | No | 57,246 |
| 19 | 18 Apr 2008 | 9.24 | 144 | No | 15,430 |
| 20 | 30 Jul 2008 | 3.39 | 42 | No | 31,220 |
| 21 | 22 Sep 2008 | 1.78 | 360 | No | 25,674 |
| 22 | 29 Jun 2009 | 9.21 | 167 | Yes | 25,315 |
| 23 | 30 Aug 2009 | 2.04 | 370 | Yes | 69,733 |
| 24 | 13 Jan 2010 | 4.47 | 293 | No | 58,767 |
| 25 | 14 Feb 2011 | 13.06 | 250 | No | 59,025 |
| 26 | 29 Jul 2011 | 5.43 | 392 | No | 39,776 |
| 27 | 16 Feb 2012 | 6.64 | 853 | No | 44,789 |
| 28 | 17 Jun 2012 | 4.01 | 300 | Yes | 50,593 |
| 29 | 24 Dec 2012 | 6.25 | 327 | Yes | 55,370 |
| 30 | 13 Feb 2013 | 1.68 | 276 | No | 43,056 |
| 31 | 8 Aug 2013 | 5.79 | 341 | Yes | 49,421 |
| 32 | 11 Aug 2014 | 12.11 | 321 | Yes | 75,697 |
| 33 | 22 Apr 2015 | 8.35 | 254 | No | 61,020 |
| 34 | 3 Sep 2015 | 4.41 | 119 | No | 40,506 |

open boundaries. Observed climatological transport (Fig. 1f) is derived from 59-month mooring data (Athie et al. 2020) and depicts a maximum increase in July of 31.4 Sv and a minimum of 24.9 Sv in March.

The mean deep circulation between 1500 and 2500 m was computed for the three experiments throughout the 19 years of simulation in order to verify or discard the presence of the large-scale circulation patterns found in observational data (Fig. 1j) (Pérez-Brunius et al. 2018; Furey et al. 2018) and other numerical studies (Morey et al. 2020; Olvera-Prado et al. 2023a). In general, OBW and OBNoW (Fig. 1g and h)

are able to reproduce the cyclonic current around the boundary of the basin, the cyclonic Sigsbee Abyssal Gyre, and the cyclone-anticyclone dipole and cyclonic circulation to the south of it, below the LC. There are, however, some significant differences in the magnitude of mean velocity between both experiments associated with the three major circulation features mentioned above, in which OBW depicts stronger velocities overall. On the other hand, the only circulation pattern present in NoOBW (Fig. 1i) is a weak Sigsbee Abyssal Gyre that is smaller in size. These results confirm that open boundary conditions, and therefore the presence of the LC

Fig. 2 Trajectories of every LCE from **a** HYCOM and **b** observations (from Donohue et al. (2008)). Comparison between OBW model control run outputs and the CMEMS database for normalized histograms of **c** LCE separation period and **d** monthly occurrence. Normalized histograms of LC northernmost latitude penetration from **e** model outputs and **f** CMEMS. Normalized histograms of LC area ($\times 10^5 km^2$) from **g** model outputs and **h** CMEMS



system, in OBW and OBNoW are responsible for the presence of these deep patterns, at least partially, and suggest that wind along with potential vorticity conservation are capable of inducing a weak cyclonic circulation in the Sigsbee abyssal plain.

2.2.2 LC and LCE metrics

Following Dukhovskoy et al. (2015), the LC and LCEs are tracked using the 0.17-m contour in demeaned SSH fields. These are calculated by subtracting the spatial mean from each SSH field record, in order to remove bias in the surface elevation fields associated with seasonal height variations due to upper-ocean warming and cooling. Then, the detachment of a LCE is defined to occur when the 0.17-m contour “breaks,” resulting in two separate contours, in which the first defines the LC and the second the detached LCE. We only consider events when eddies detach and ultimately dissipate, which are commonly known as separation events. The date of each LCE separation event is when the 0.17-m LC tracking contour breaks (Leben 2005; Dukhovskoy et al. 2015). From the objective tracking technique applied to the 19-year record of SSH, a total of 34 separation events were identified, yielding a mean LCE separation period of 6.8 months. The main characteristics of the 34 LCEs are listed in Table 2. The propagation trajectories of the 34 LCEs are shown in Fig. 2a, which show good agreement with observations (Fig. 2b) (Donohue et al. 2008). The normalized histograms of the distribution of LCE separation events and number of separation events by month from the model are shown in Fig. 2c and d respectively (blue bars) along with the corresponding histogram from the CMEMS database (red lines). In general, there is good agreement between the distribution of the LCE separation period derived from the model and from observations, both depicting asymmetric, positively skewed distribution of the data. The mean LCE separation period from observations is 7.1 months. The seasonal distribution of separation events from the model and observations show two relative peaks, one in winter/spring and another in summer.

LC metric statistics based on the tracking of the 0.17-m SSH contour were derived from the 19-year simulation data and the 28-year CMEMS SSH dataset, to be directly compared between them. The normalized histograms of the LC northernmost latitude reveal unimodal distributions in both cases, with the peak centered on the 27.4–27.6° N bin and a mean on 26.9° N for the model (Fig. 2e), and the peak centered on the 26.8–27° N bin and a mean on 26.3° N for the observations (Fig. 2f). The distribution of the LC area in the model and altimeter-derived data also depicts unimodal distributions, with the mode centered on 180,000–190,000 km² and the mean on 163,021 km² for the model (Fig. 2g), and the mode centered on 140,000–150,000 km² and the mean on 133,226 km² for the observations (Fig. 2h).

2.2.3 Kinetic energy of the deep flow

The eddy kinetic energy per unit mass (EKE) and the kinetic energy per unit mass of the mean flow (MKE) from the model velocity time series (u , v) at each model grid point, between 1500 and 2500 m, were analyzed and compared with the corresponding quantities derived from the binned float velocities by Pérez-Brunius et al. (2018) and presented in Morey et al. (2020). EKE is computed as follows:

$$EKE = \frac{1}{N} \sum_{i=1}^N \frac{[(u_i - \bar{u})^2 + (v_i - \bar{v})^2]}{2} \quad (1)$$

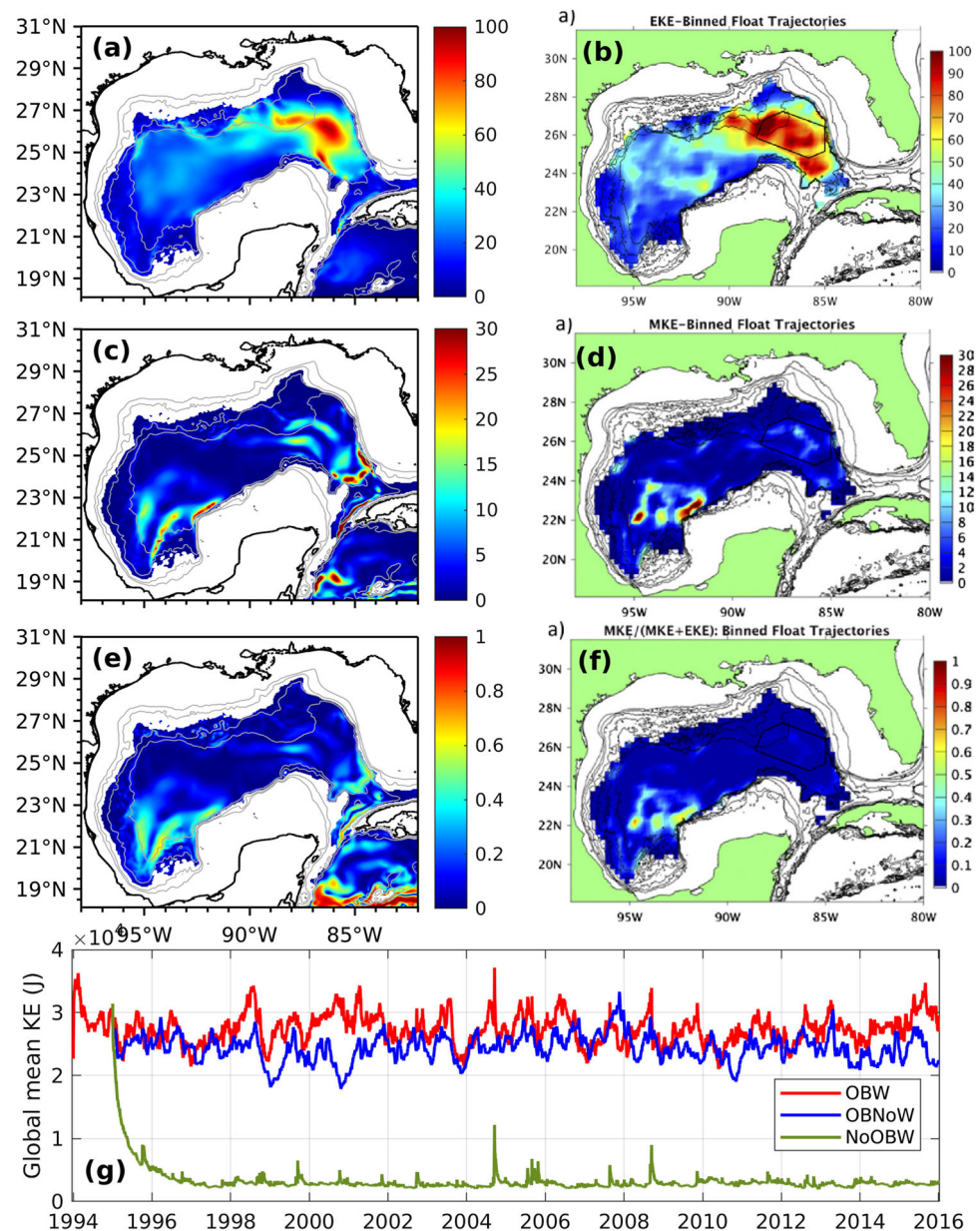
and MKE is computed as follows:

$$MKE = (\bar{u}^2 + \bar{v}^2)/2 \quad (2)$$

where (\bar{u}, \bar{v}) are the mean velocity vectors, and N is the length of the time series. In general, the model simulates weaker variability of the velocity in the deep layer of the GoM, as quantified by the EKE (Fig. 3a), than observed by the floats (Fig. 3b). Both datasets depict enhanced EKE in the eastern part of the basin compared to the western part, but with the EKE of the binned float velocities showing higher magnitude and covering a wider region. Inspection of the MKE fields shows that in the Sigsbee Abyssal Gyre, the model (Fig. 3c) presents similar magnitude to that computed from the float trajectories (Fig. 3d), but in the model, this feature extends southward and westward towards the Bay of Campeche including which appears to be the bottom boundary current, whereas the observations show a distinct separation between both features. Also, the model shows a region of high MKE along the northwestern Campeche Bank in agreement with observations.

Finally, as in Pérez-Brunius et al. (2018), the ratio of MKE to the total kinetic energy, $MKE/(MKE + EKE)$, is computed in the model data as an indicator of the relative persistence of the mean circulation (Fig. 3e), and compared to the corresponding ratio derived from the binned float velocities (Fig. 3f). In general, both datasets show similar behavior and magnitude, and the Sigsbee Abyssal Gyre is highlighted by larger values of this quantity due to its relative persistence. Low values in the eastern GoM are also present, suggesting that the eddy structure under the LC region, namely, the anticyclone-cyclone dipole and the cyclone to the south of it, is highly variable. The cyclonic boundary current branch within the BoC also appears to be a persistence feature around most of the basin evident only in the long-term mean.

Fig. 3 EKE ($\text{cm}^2 \text{s}^{-2}$) derived from **a** the model (OBW) and **b** the observed float velocities (from Morey et al. (2020)), MKE ($\text{cm}^2 \text{s}^{-2}$) derived from **c** the model (OBW) and **d** the observed velocities (from Morey et al. (2020)), the ratio of MKE to the total kinetic energy per unit mass [$\text{MKE}/(\text{MKE} + \text{EKE})$] derived from **e** the model (OBW) and **f** the observed velocities (from Morey et al. (2020)), and **g** the time evolution of the global kinetic energy in the model domain (J) from experiments OBW (red line), OBNoW (blue line), and NoOBW (green line)



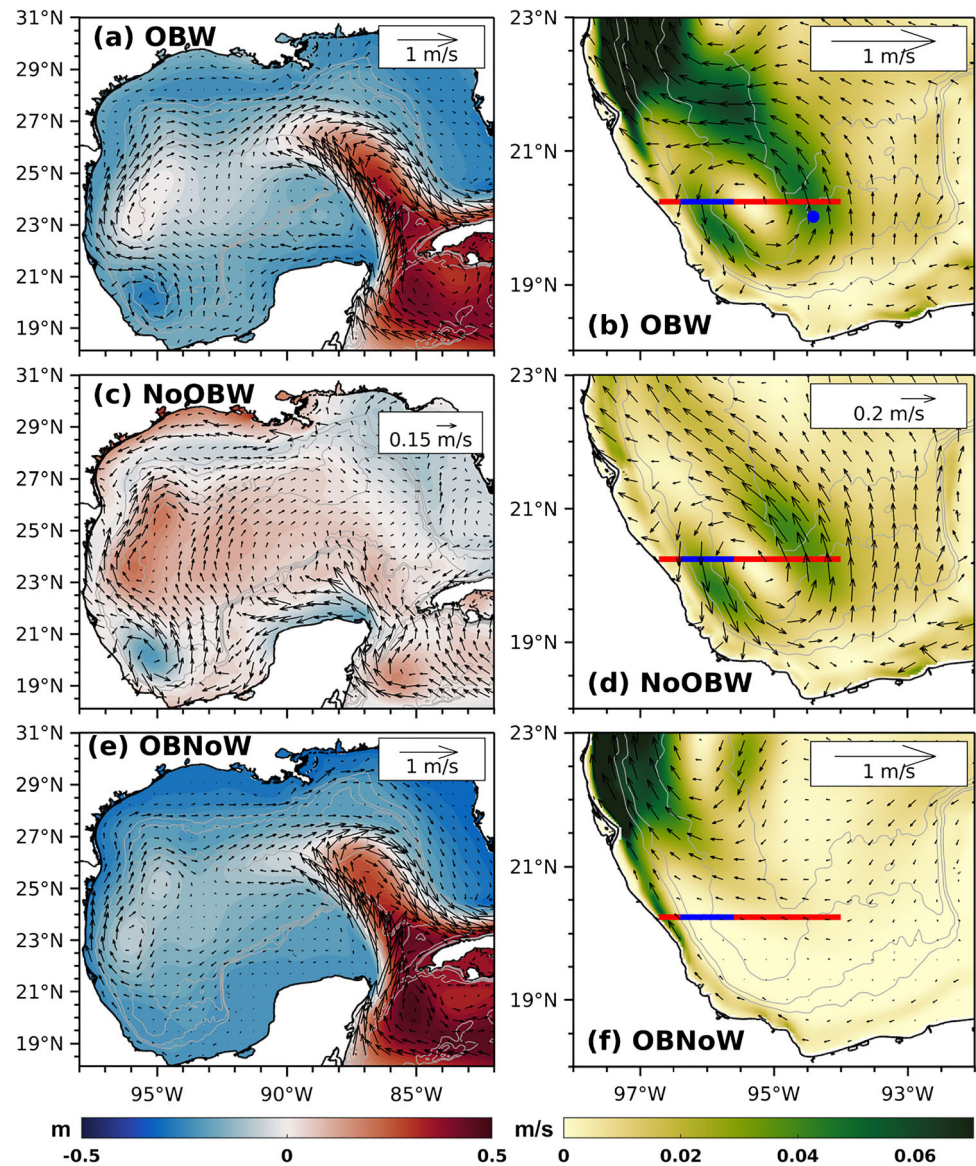
3 Results

3.1 Mean circulation and vertical structure

This subsection quantifies the mean contribution of the wind stress and LCEs to the CG circulation by examining the mean velocity fields obtained through the 19 years of simulation. Figure 4 shows the mean surface velocity field and SSH anomalies over the whole domain, including a zoom over the BoC showing velocity vectors and speed contours for the three experiments. Among the main features that can be observed are the following: experiment OBW (Fig. 4a) depicts the Loop Current at an “intermediate” stage over the eastern GoM, and a broad anticyclonic circulation over the

central- and north-western regions, commonly referred to as the Western Anticyclonic Gyre, located from 88° W to the west and from ~22°N to the north of the domain, represented by small negative SSH anomalies after demeaning. To the west of the BoC, the CG is shown centered at around 95.5° W and 20.25° N and is represented by negative SSH anomalies. The mean circulation in NoOBW (Fig. 4c) shows the Western Anticyclonic Gyre as well as the CG in the BoC, although the latter is slightly weaker and centered to the south compared to OBW. Experiment OBNoW (Fig. 4e) shows a narrow area of high pressure on average extending from the LC through the central-western region, which mimics the south-west mean trajectory of LCEs (Vukovich 2007). Unlike OBW and NoOBW, OBNoW does not present any

Fig. 4 **a, c, and e** Mean surface velocity vectors and SSH anomalies for the experiments OBW, NoOBW, and OBNoW in the model domain. **b, d, and f** Surface velocity vectors and speed contours zoomed in the BoC, where the red line indicates the zonal section where statistics of the meridional velocity were calculated, the blue line is the zonal section where the transport was calculated, and the blue dot in **b** shows the location where the vertical coherence of the currents were estimated. The gray contours indicate the 500, 1000, 2000, and 3000 m isobaths



signature of a cyclonic circulation in the BoC, at least not on the surface, which suggests the strong dependence of the surface component of the CG on the wind forcing. Zoom in the BoC shows strong mean speed values in the western and eastern arms of the CG for OBW and NoOBW (Fig. 4b and d); however, high speed values are also found to the north of the BoC in OBW, which is related to the continuous presence of LCEs in the western GoM, as shown in Figs. 2 and 8. As a consequence, the CG in OBW appears to be flattened by them, compared to NoOBW, in which the CG is less disrupted from its unperturbed state and therefore presenting a stretched-out shape.

In order to examine the vertical structure of the CG, a zonal section at 20.2° N and between 96.7° W and 94.0° W (red line Fig. 4b) was defined as representative of the CG core. The mean meridional velocity in this section is

shown in Fig. 5a–c for the three experiments. It is observed that for OBW and NoOBW, velocities are surface-intensified ($\sim 0.1 - 0.2 \text{ ms}^{-1}$), but for OBW, the magnitude decreases steadily up to ~ 1000 m, while for NoOBW, the Gyre seems to be confined within the upper ~ 600 m. In experiments OBW and NoOBW, the center of the CG is located around 95.3° W and depicts a nearly symmetric shape with similar speed magnitude in the western and eastern arms. Additionally, a revealing characteristic is that in OBW, the signal of a cyclonic circulation extends below 1000 m, with weaker but steady velocities ($\sim 5 \text{ cms}^{-1}$) throughout the water column to the bottom of the basin.

The mean velocity section for OBNoW (Fig. 5c) depicts a weaker, yet symmetric, net cyclonic circulation above 1000 m, a revealing result considering that in this experiment, the BoC is solely under the influence of LCEs. Also

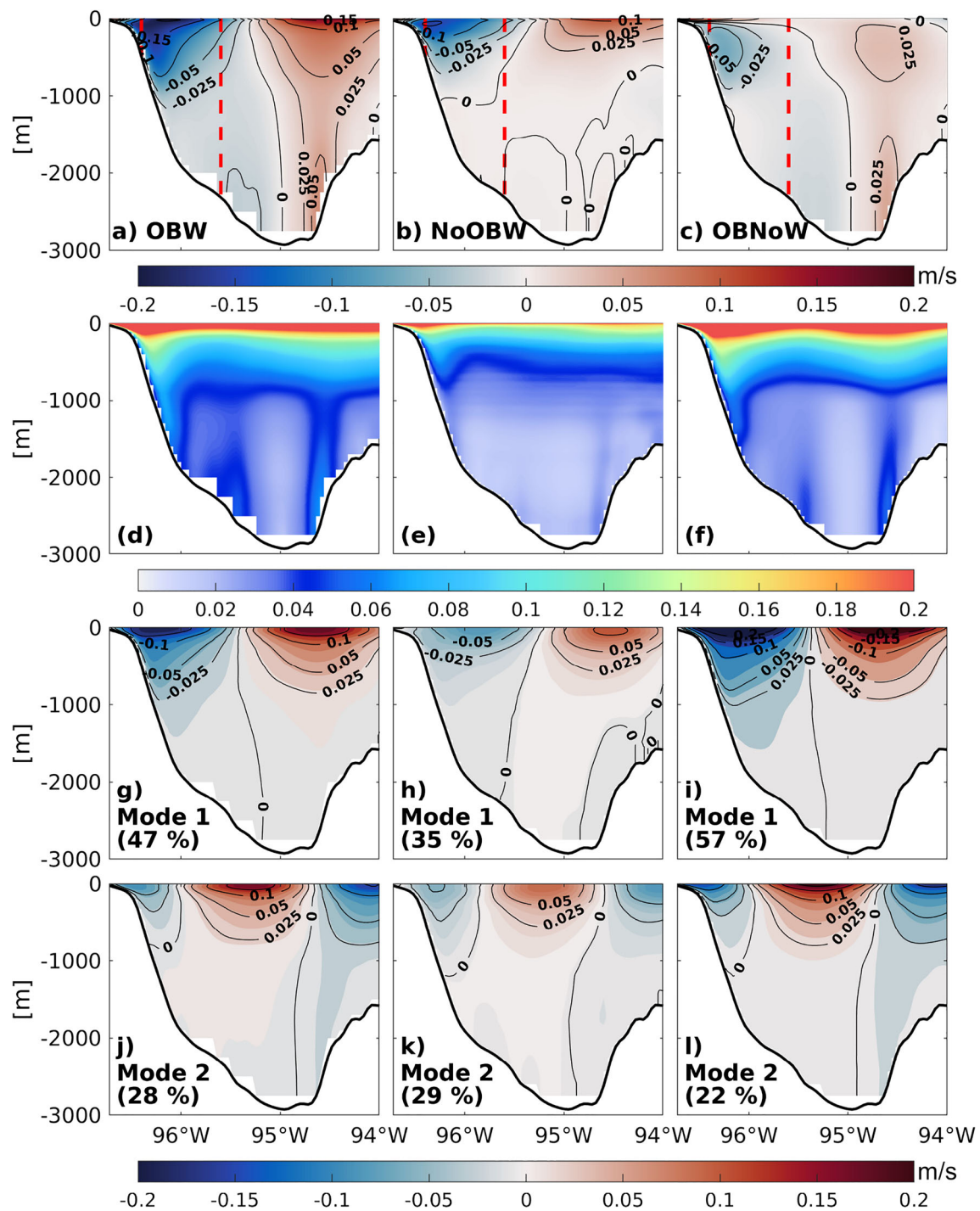


Fig. 5 Mean (a–c) and standard deviation (d–f) of meridional velocity (positive northward) in the CG (at 20.2° N) for the experiments OBW, NoOBW, and OBNoW; the vertical red dashed lines in a–c limit the section where transport was computed. First (g–i) and second (j–l) EOF

modes of the meridional velocity for the three experiments. In general, EOF-1 explains ~ 35–57% of the variance and EOF-2 ~ 20–30% in the three experiments

noticeable is the fact that below 1000 m depth, the structure and magnitude of the cyclonic circulation are present in experiments OBW and OBNoW, suggesting that this feature is the expression of a separate circulation feature intrinsically related to the LC system. One such candidate is the cyclonic boundary current flowing around most of the deep perimeter of the GoM, reportedly to be located between the 2000- and 3000-m isobaths in observational (Pérez-Brunius et al. 2018) and numerical (Morey et al. 2020) studies. Such studies suggest that this deep current is episodic in character, with long periods of cyclonic flow and shorter periods of back-and-forth motion associated with a dominant time scale of ~ 14 months, whose variability within the BoC could be related to the coupling between the upper and lower layers of the GoM when a LCE traveling westward, reach the western boundary (Furey et al. 2018; Olvera-Prado et al. 2023a). We have shown that such a deep feature is indeed well resolved in both experiments (Fig. 1g and h); furthermore, the standard deviation of the flow for both experiments (Fig. 5d and f) shows small variability in the cores of the cyclonic circulation between ~ 1500 and 3000 m which can be associated with the persistence of the current and the findings mentioned above.

The vertical spatial structure of the CG flow variability in the three experiments is well explained by their first two empirical orthogonal function (EOF) modes (Fig. 5g–i). The first mode depicts a dipole pattern with negative and positive signs in the western and eastern cores respectively in the three experiments, similar to the mean velocity pattern, explaining between ~ 35 and 57% of the total variance. This mode seems to describe the intensification and weakening of the CG in the upper ~ 1000 m resulting from the variability imposed by the wind (NoOBW), the LCEs (OBNoW), or both (OBW). As expected from the mean meridional velocity structure at the zonal section (Fig. 5a–c), variability in the first mode is stronger in experiments OBW and OBNoW, where the BoC is influenced by LCEs. The second mode, explaining between ~ 20 and 30% of the total variance, displays a tripole pattern in the three cases, with the center core probably related to the longitudinal displacement of the center of the CG. The above is in general agreement with the findings of Pérez-Brunius et al. (2013), in which the variability of the surface currents in the western basin is primarily due to changes in the size, form, position, and intensity of the CG due to its interaction with LCEs.

Our results for the three experiments show that, on average, a nearly symmetric cyclonic gyre is present in the western BoC, although with some differences in the vertical extension and strength among these experiments (Fig. 5a–c). In addition, the EOF analysis applied to the vertical structure of the flow in the CG shows that the major mode of variability is consistent with a dipole pattern similar to the mean state but confined to the upper 1000 m (Fig. 5g–i). The above sug-

gests that the location of the CG and its principal variability is influenced by a common factor present in the three cases. The implications of these facts are relevant. Previous studies indicate that the CG flow can be modeled as equivalent barotropic (Pérez-Brunius et al. 2013; Zavala Sansón 2019), with the particular topography of the basin and the equivalent depth of the flow resulting in closed potential vorticity contours f/F_0 to the west of the BoC, where f is the Coriolis parameter, $F_0 = H_0(1 - e^{-H/H_0})$, H_0 is the equivalent depth, and H is the total depth. Then, the conservation of potential vorticity forces the current to follow such contours in the absence of forcing and dissipation (Pedlosky 1987). Furthermore, in the presence of realistic wind forcing, this flow can be stronger and present seasonal variability, consistent with our findings for OBW and NoOBW.

3.1.1 The role of topography under different dynamic conditions

We explore the role of topography under these different dynamic conditions by evaluating if the flow is equivalent-barotropic in the three experiments. We adopted an approach similar to Pérez-Brunius et al. (2013) and used two different methods to estimate the equivalent depth from the velocity profile in the model on the eastern flank of the CG (blue dot in Fig. 4b). Such a location is the closest to the CTZ mooring of Pérez-Brunius et al. (2013) (their Fig. 3b); we consider this location more appropriate for the evaluation since the continental slope does not directly influence it. First, the complex correlation coefficients (Kundu 1976) between the mean model velocity at 40 m and the velocities at deeper depths were computed; the depth at which the coefficient exceeds 90% was taken as a proxy at which velocities are still correlated with the currents at 40 m. Figure 6a, d, and g show the vertical profile of mean horizontal currents for OBW, NoOBW, and OBNoW, respectively. For OBW and OBNoW, the flow is approximately unidirectional from the surface to 820 and 920 m depth, respectively. In both cases, below this depth, the flow rotates clockwise to the east, which seems to be the signature of the bottom boundary current. For NoOBW, the coherent upper layer thickness is about ~ 450 m, which is shallower than the other two cases.

The second method to estimate the equivalent depth considered an EOF analysis of the mean vertical velocity profiles. EOFs of the velocity profile, including their mean, were estimated to obtain the first mode of vertical variability. Figure 6b, e, and h show the eigenvector for the first EOF mode for the three experiments. In all the cases, the first mode explains $> 80\%$ of the total variance. It can be seen that the vertical structure for all three cases depict unidirectional velocities from the surface up to ~ 800 – 1000 m. After adjusting the function $v(z) = v(0)e^{(z/H_0)}$ to the first modes of vertical variability, we obtain an e-folding scale of $H_0 \sim 950, 800,$

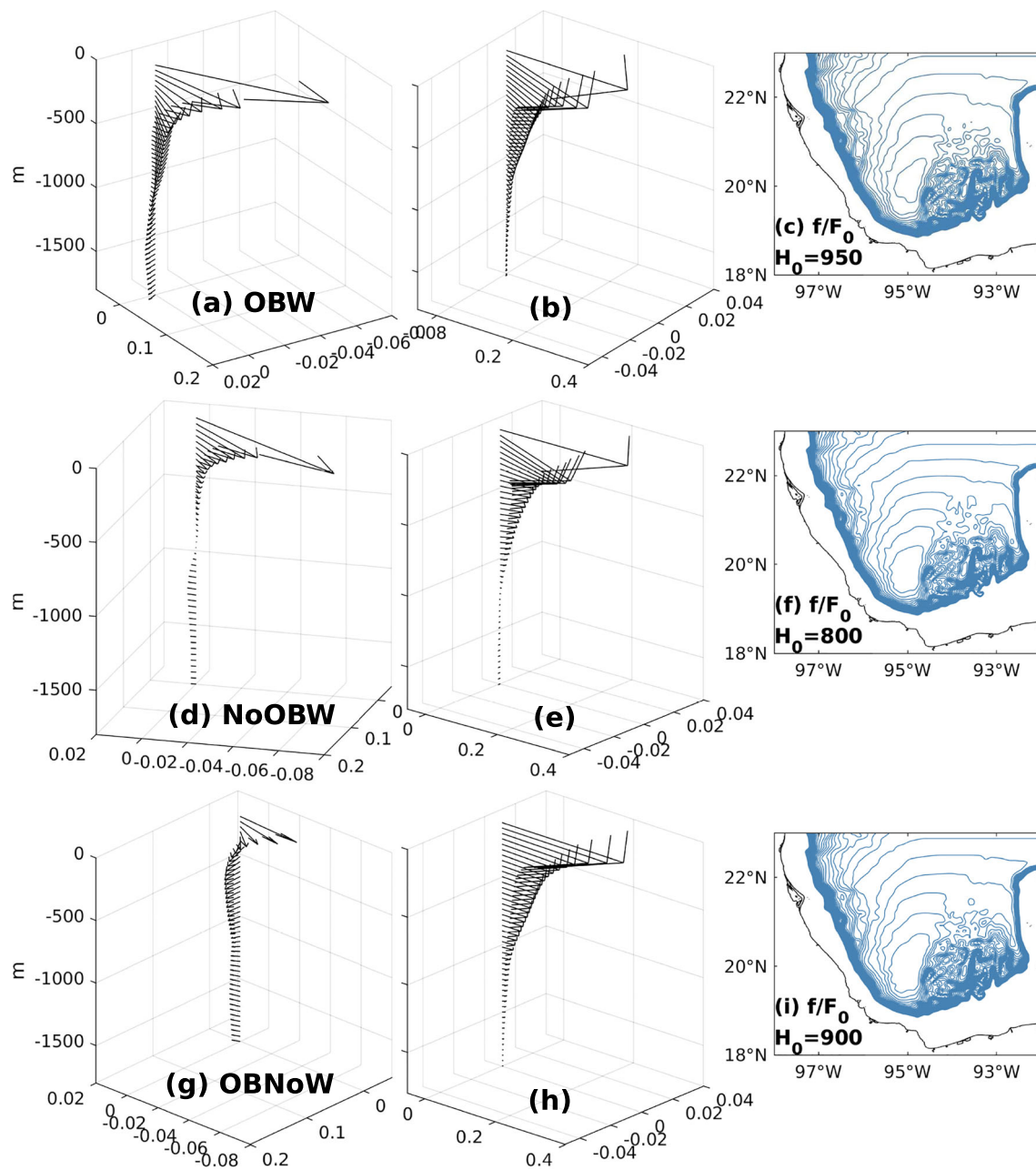


Fig. 6 Vertical profiles of mean horizontal currents and first modes of vertical variability for experiments **a** and **b** OBW, **d** and **e** NoOBW, and **g** and **h** OBNoW respectively. Also shown are the geostrophic contours f/F_0 ($[4:0.1:10] \times 10^{-8} m^{-1}/s^{-1}$) with f the local Coriolis parameter,

$F_0 = H_0(1 - e^{-H/H_0})$, H the bottom depth and equivalent depths of (c) $H_0 = 950$ m for OBW, (f) $H_0 = 800$ for NoOBW, and (i) $H_0 = 900$ for OBNoW

and 900 m for OBW, NoOBW, and OBNoW respectively. See Table 3 for the results of the evaluation of the vertical coherence of the flow using both methods. Finally, we plotted the geostrophic contours (f/H_0) for the resulting equivalent depths using the EOF method and found that in the three cases, the contours are closed in the western BoC (Fig. 6c, f, and i). These findings indicate that regardless of wind, LCEs, or both, the flow in the western BoC is equivalent-barotropic,

and hence, the location of the gyre is given by the particular topography of the basin, thus corroborating the importance of the topography in steering equivalent-barotropic flows.

3.2 Seasonal modulation of the Campeche Gyre

The seasonal modulation in the western and southern GoM has been partially addressed previously, mainly using obser-

Table 3 Results of the evaluation of vertical coherence of the flow derived from a velocity profile in the model close to the CTZ mooring in Pérez-Brunius et al. (2013). First row shows the equivalent depth using the complex correlation method between the mean currents at 40m and the currents at different depths, in particular the maximum depth for which $R \geq 0.90$. Second row shows the equivalent depth H_0 after adjusting the function $v(z) = v(0)e^{(z/H_0)}$ to the first modes of vertical variability

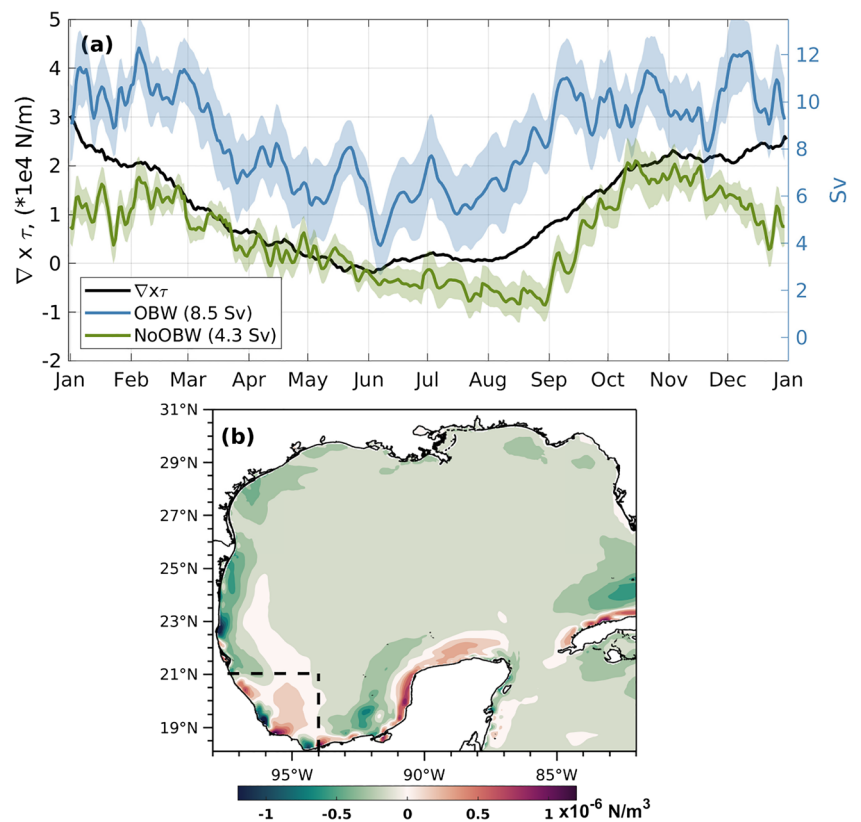
| Method/experiment | OBW | NoOBW | OBNoW |
|-------------------|-----|-------|-------|
| Mean velocity (m) | 820 | 450 | 920 |
| EOF (m) | 950 | 800 | 900 |

variations (Pérez-Brunius et al. 2013; Vázquez et al. 2005). The current consensus is that the wind plays a dominant role, but there might be other processes influencing the seasonal variability of the CG, such as the interaction with LCEs. Consequently, an in-depth analysis is needed. In this section, we examine the relationship between the seasonal components of the wind stress curl and the transport through the western arm of the CG in the presence and absence of LCEs. To this end, a zonal section was defined in the CG at 20.2° N and between 96.4° W and 95.6° W (blue line in Fig. 4b and d). Then, the daily transport was computed from the surface to the bottom of the section (dashed lines in Fig. 5a), and annual climatologies were estimated for experiments OBW and NoOBW. The positive transport is defined southward

in the section. Figure 7a shows these time series along with the annual climatology of the wind stress curl (black line in Fig. 7a) averaged over the western BoC (dashed lines in Fig. 7b). In both experiments, the climatological transports display a strong seasonality, with high values during fall and winter and low values during spring and summer. The mean and standard deviation of the transport in OBW (8.5 Sv, $\sigma = 7.1$ Sv) are higher than in NoOBW (4.3 Sv, $\sigma = 3.6$ Sv). We attribute the difference in the means to the contribution of the deep boundary current to the transport in OBW. As expected, the wind stress curl also displays strong seasonality within the western BoC, with high positive values during fall and winter and low values during spring and summer. High Pearson’s correlation coefficients (R) between the wind stress curl and the transport in OBW (R=0.81) and NoOBW (R=0.83) suggest a possible physical association and a causal relationship between them.

In order to evaluate if it is physically plausible that the seasonal cycle of the transport in the CG is driven by wind stress curl, we computed the correlation lag (using Pearson’s correlation) between both time series. According to Sturges (1993), long Rossby waves in the GoM travel at approximately 4 km/day; therefore, the short distances involved in this study result in advective time scales of a few days to weeks, which corresponds to the expected ocean response to wind forcing. For NoOBW, the correlation remains high (R

Fig. 7 **a** Annual climatology of the transport through the western arm of the CG computed in a zonal section (blue line in Fig. 4) for experiments OBW and NoOBW, where the shading area represents the standard error; OBW and NoOBW share the right axis. **b** Mean wind stress curl over the GoM; the region within the dashed limits is where the time series of the average wind stress curl was calculated and plotted in **a**



> 0.8) within the first 20 days of lag, with a peak at 15 days. After this time, the correlation drops abruptly. For OBW, the correlation is maximum after ~ 5 days ($R = 0.85$), and then it decreases abruptly. In both cases, the wind precedes the transport.

These results are statistically consistent enough to prove a major characteristic of the circulation in the BoC, the dominant role of the wind in modulating the seasonal variability of the CG, a feature that was speculated in previous observational studies like Vázquez et al. (2005) and Pérez-Brunius et al. (2013). The higher standard error (blue shading Fig. 7a) of the transport in OBW suggests that a primary effect of LCEs on the CG circulation is that they impose higher fluctuations in the transport field. Nevertheless, these fluctuations do not seem to affect the seasonal component of the circulation but rather the non-seasonal component. This effect is addressed in detail in the following section.

3.3 Non-seasonal modulation of the Campeche Gyre

The presence and distribution of the higher fluctuations in the climatological transport in the CG for experiment OBW, compared to NoOBW (Fig. 7a), suggest that LCEs can reach the southwestern boundary of the GoM in virtually any season of the year, contributing to the non-seasonal variability of the BoC circulation. In order to examine in more detail the mechanism by which LCEs influence the CG circulation considering a long record of events, we analyzed the trajectories of the 34 LCEs separated from the LC in experiment OBW (Fig. 2a) and identified 17 LCEs that followed a southern path (Vukovich 2007), reaching the northern BoC. The trajectories of the 17 LCEs are shown in Fig. 8a, whose centers are at any given moment in waters deeper than 2000 m. Then, from visual inspection of the surface velocity and SSH fields

during these events, time periods when the LCEs presented a large southward penetration and whose accompanying eddy field influenced the BoC were recorded. Such periods of time are highlighted in orange in the trajectories of Fig. 8a; note that most of the events are located south of 23.5° N. To get a representation of the average conditions in the BoC when eddies interact with the CG, a composite of surface velocity and SSH fields was constructed by computing the mean of these fields over such time periods (Fig. 8b). The composite shows a LCE centered around 95.75° W and 22.5° N with its southern rim reaching 21.5° N, influencing the northern boundary of the BoC. This southward penetration appears to result in a reduction in size and a displacement towards the southwest of the mean CG compared to its annual average conditions (Fig. 4b).

Individual events can be first addressed by inspecting the daily time series of transport through the entire 19-year simulation. Figure 9a (upper panel) shows such time series for experiment OBW with the periods of time when LCEs influenced the BoC highlighted in orange and green, along with the principal component of the first EOF of the meridional velocity through the zonal section shown in Fig. 5g. In addition, a wavelet power spectrum was computed for the corresponding transport (lower panel of Fig. 9a) following Liu et al. (2007) in order to see the time scales of variability. It is observed that in some of the events of LCE southern penetration, the transport through the CG decreases, reversing it in some cases (orange color); in some other events, a decrease in the transport is followed by an increase (green color), with all cases distinctly contributing to the intraseasonal variability of the CG circulation. Furthermore, the principal component is very similar to the corresponding transport ($R=0.79$), especially in events of LCE penetration into the BoC. The wavelet analysis shows two prominent peaks of energy: one major

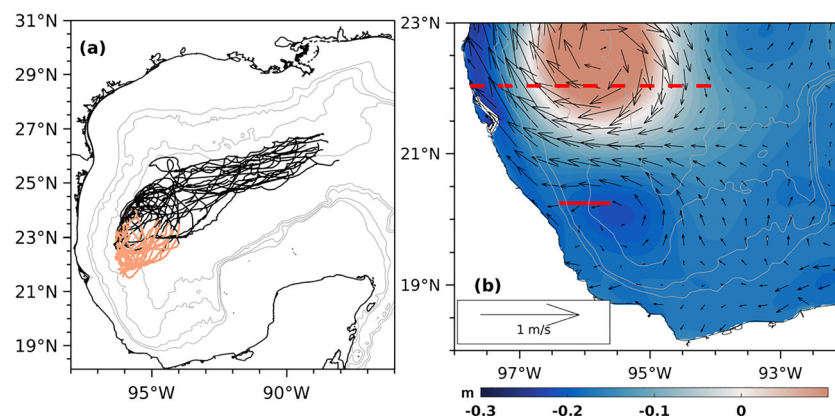
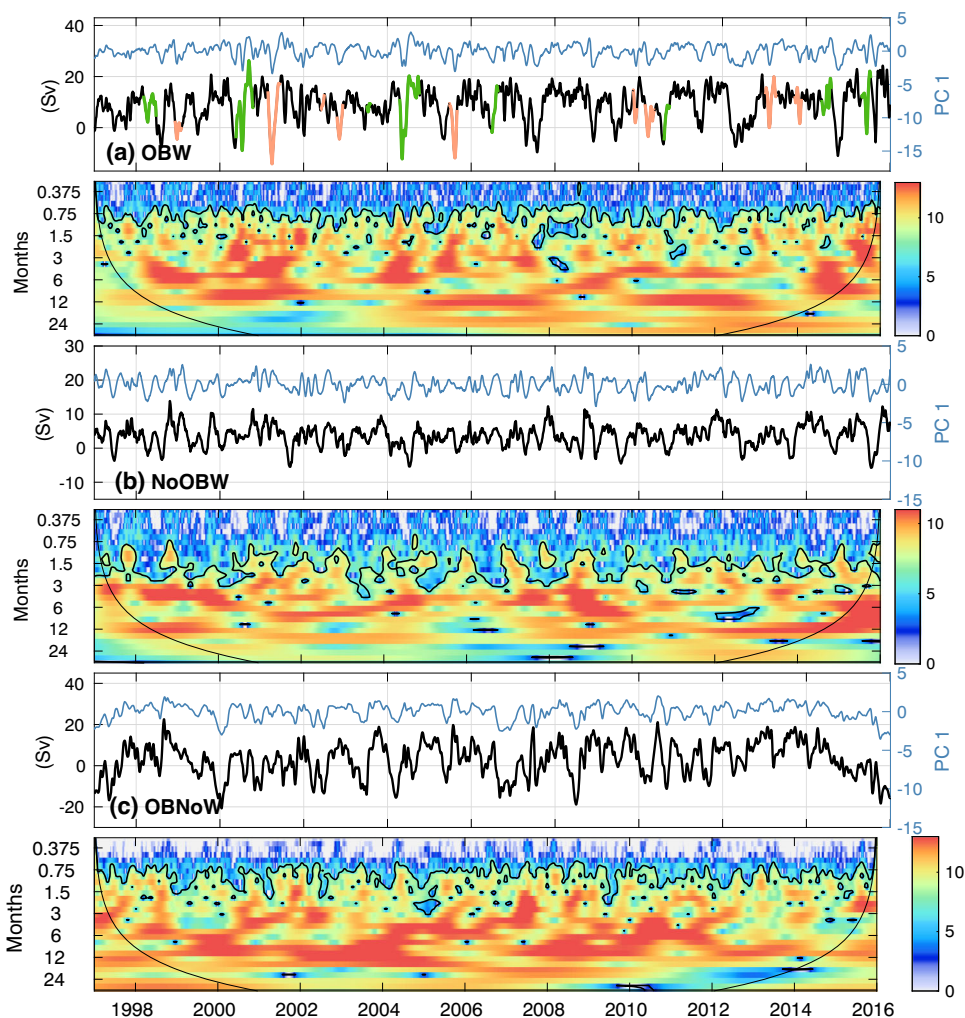


Fig. 8 **a** Trajectories of the 17 LCEs that followed a southern route and passed near the BoC for experiment OBW; time periods when LCEs interacted with the CG are highlighted in orange. **b** Composite of the surface velocity vectors and SSH contours when LCEs interacted with

the CG; the red dashed line indicates the zonal section where the vorticity flux computation was done and the red continuous line the section where the transport was computed. The gray contours indicate the 500, 1000, 2000, and 3000 m isobaths

Fig. 9 Time series of daily transport (black lines) through the western boundary current in the CG for experiments **a** OBW, **b** NoOBW, and **c** OBNoW and their respective wavelet power spectrum. The regions with greater than 90% confidence are shown with black contours, and the “cone of influence,” the region where edge effects become important, is also indicated. In **a**, time periods when the LCE influence the CG by decelerating it are highlighted in orange, and time periods when the cyclone accompanying the LCE entered the BoC and intensified the CG are highlighted in green. The principal component of the first EOF mode (blue lines) of the meridional velocity through the zonal section in Fig. 5 is also shown for the three experiments



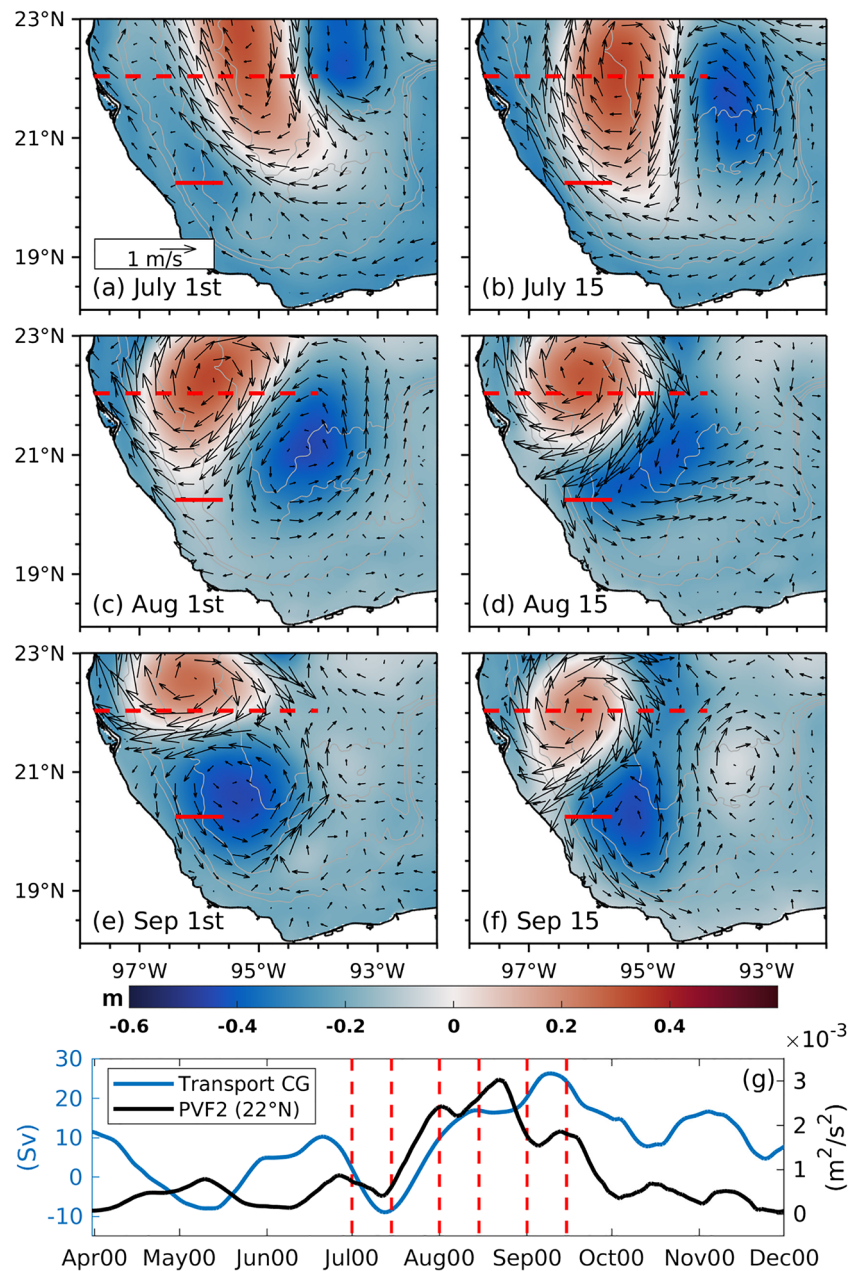
peak at around 5 months, distinctly related to the duration of the interplay between the LCEs and the CG, and one minor peak at 12 months, related to the annual signal, which is more energetic in periods with absence of LCEs in the BoC, e.g., years 2011–2012.

The transport in experiment NoOBW (Fig. 9b) displays a smaller mean (4.3 Sv) and shorter fluctuations with a marked seasonal signal, which is regular throughout the period. As in experiment OBW, the variability of the principal component of the first mode is very similar to that of the transport ($R=0.73$). The wavelet analysis shows a substantial peak of energy at 12 months and a minor peak at 6 months. Finally, the computed daily transport in experiment OBNoW (Fig. 9c) shows a low mean and high standard deviation (3.4 Sv, $\sigma = 8\text{Sv}$), with a high intraseasonal signal related to the arrival of LCEs in the southwestern GoM. The variability of the principal component of the first mode is very similar to that of the transport ($R=0.9$). The global wavelet spectrum shows substantial variability on time scales from 3 months to 2.0 years, with two prominent peaks of energy at periods around

5 and 12 months, clearly related to the presence of LCEs in the BoC.

To further examine the circulation in the BoC during the influence of LCEs, we made a movie which includes the time evolution of the daily SSH and surface velocity field in the BoC, the meridional velocity in the CG zonal section (Fig. 4b), and the time series of daily transport through the CG western arm (online supplemental material). After examining the movie, we identified two main types of events leading to the particular GC behavior mentioned above. A good example of the first type of event takes place in 2000 (Fig. 10), when a LCE started influencing the northern boundary of the BoC by July (Fig. 10a), producing weak southward currents in the upper $\sim 1000\text{m}$ of a weak CG (blue line Fig. 10g). In mid-July (Fig. 10b), the LCE shows a large southward penetration into the BoC, replacing the CG and producing the reversals in transport sign (Fig. 10g). During this period of time, a big, strong cyclone is also observed accompanying the LCE to its east. Then, at the beginning of August, the cyclone starts entering the western BoC (Fig. 10c), where it eventually

Fig. 10 a–f Snapshots of SSH and velocity fields for an event in model year 2000 where the BoC is influenced by a LCE and a cyclone. Each frame is separated by ~ 15 days. The continuous red line indicates the zonal section where the transport was integrated ($\sim 20^\circ$ N), and the dashed red line indicates the zonal section where the PV flux was computed ($\sim 22^\circ$ N). **g** Time series of transport through the section at 20° N (blue line) and of the PV flux through the section at 22° N (black line); red vertical dashed lines indicate the times of the snapshots for frames a–f

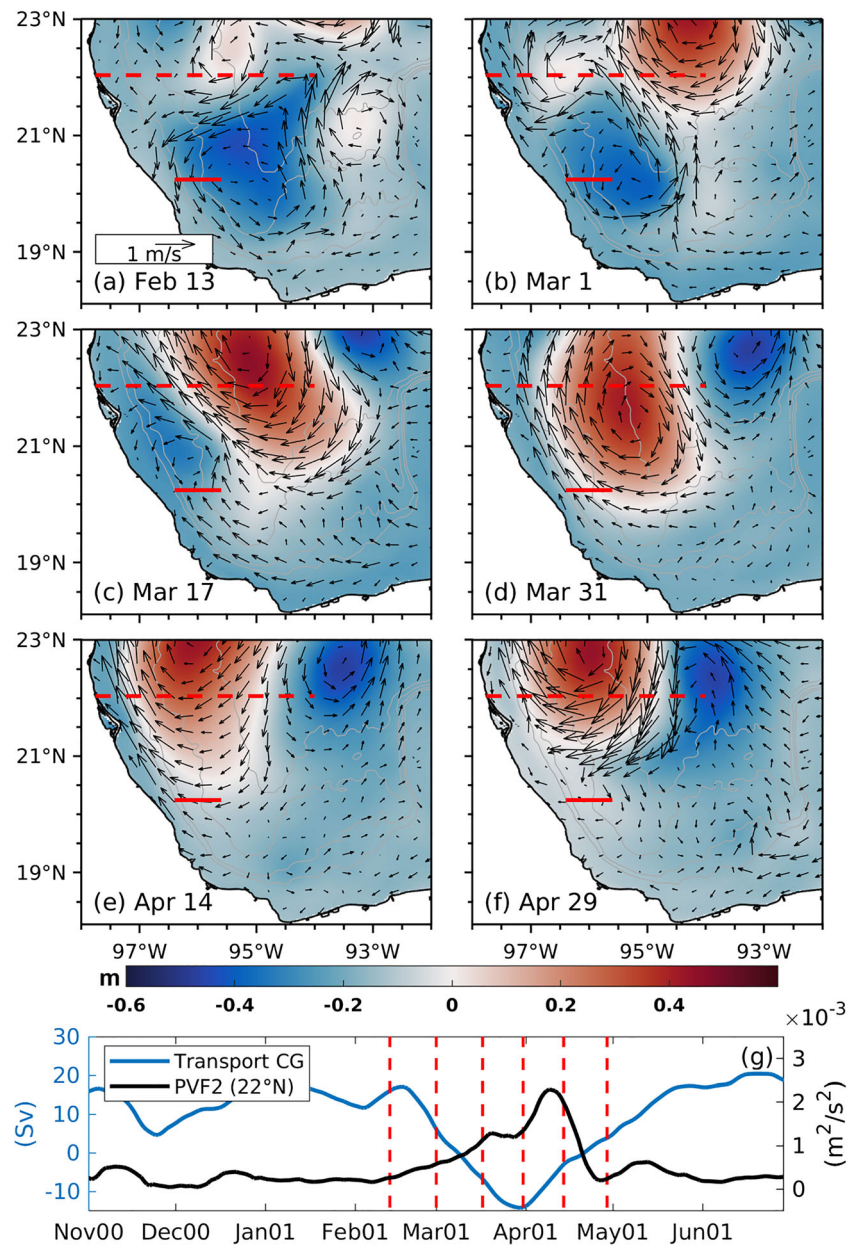


acts to reinforce and intensify the remains of the previously disrupted CG while the LCE moves northward (Fig. 10d). As a consequence, the transport significantly increases in these stages (Fig. 10g). Finally, during the following months, the CG relatively maintains the same strength until the next LCE arrives in the region (Fig. 10e and f). After reviewing the rest of the events in the movie, it was found that the mechanisms described above operate in 8 of the 17 events of LCE southern penetration (green in Fig. 9a), that is, an initial disruption of the CG upon the arrival of a LCE and its subsequent re-intensification produced by a cyclone entering the region. In addition, it is important to note that in periods without LCEs, e.g., from 2008 to 2009 or 2011 to 2012, smaller-in-size anti-

cyclones locally generated in the BoC also interact with the CG, producing small perturbations in the transport.

An example of the second type of event occurred in 2001 (Fig. 11), following the previously analyzed event. In this case, the LCE arrives at the western GoM in mid-February, when a strong cyclonic circulation is present in the western BoC (Fig. 11a). As the LCE starts to move further south at the beginning of March, it decelerates and disrupts the CG, reducing the transport through its western side (Fig. 11b). Then, during the following weeks, the LCE presents a large southward penetration into the BoC, reducing the size of the CG until its disruption (Fig. 11c), eventually producing the reversal in transport when the LCE replaces the inhibited

Fig. 11 a–f Snapshots of SSH and velocity (vectors) for an event in model year 2001 where the BoC is influenced by a LCE. Each frame is separated by ~15 days. The continuous red line indicates the zonal section where the transport was integrated (~20° N), and the dashed red line indicates the zonal section where the PV flux was computed (~22° N). **g** Time series of transport through the section at 20° N (blue line) and of the PV flux through the section at 22° N (black line); red vertical dashed lines indicate the times of the snapshots for frames a–f



CG (Fig. 11d). In April, the LCE moves northward, leaving a relatively calm region and weak currents in the western BoC (Fig. 11e and f). These findings indicate that the mechanisms by which LCEs influence the BoC circulation is more complex than previously stated, confirming that the hypotheses about the intensification of the CG (Vidal et al. 1992; Vázquez et al. 2005) and its disruption (Pérez-Brunius et al. 2013) upon the arrival of LCEs are both true.

From examining the influence of LCEs on the BoC circulation in OBW, we learned that in approximately half of the events (8), LCEs arrive at the northern BoC accompanied by a cyclone that eventually enters the western BoC and strengthens the CG. The same process is expected to happen in OBNoW. In that sense, we still have to find an explana-

tion for the fact that, in the absence of wind forcing, a weak, net cyclonic circulation in the upper layer (<1000 m) of the western BoC is formed on average for OBNoW (Fig. 11c). This suggests that LCEs and their associated eddy field are capable of inducing a “weak” CG, a process that, according to our results for OBW, seems plausible.

3.3.1 Vorticity flux through the Bay of Campeche

The Ertel’s potential vorticity (PV) is an expression that can be used as a tracer of large-scale ocean circulation since it combines the laws of conservation of mass and angular momentum. Several authors have used Ertel’s PV to study the vorticity flux through different water bodies using obser-

variations, elucidating the origins of the different water masses and understanding the conditions under which certain processes take place (e.g., Beal and Bryden (1999); Candela et al. (2002, 2003); Oey et al. (2004). The examination of the vorticity flux through the BoC provides a way to understand how the vorticity is transferred into or out of the BoC when LCEs and its associated eddy field interact with the CG, as well as to analyze further previous hypotheses based on observations.

The simplified Ertel’s PV for a stratified fluid is as follows:

$$q \approx - \left[f \frac{\partial \rho}{\partial z} + \frac{\partial v}{\partial x} \frac{\partial \rho}{\partial z} - \frac{\partial v}{\partial z} \frac{\partial \rho}{\partial x} \right] / \rho_0 = q_1 + q_2 + q_3 \quad (3)$$

where u and v are the x and y components of the velocity and z the vertical coordinate (positive upwards), ρ_0 is a reference mean density, ρ is potential density, and f is the Coriolis parameter. The first term on the right-hand side is the planetary vorticity multiplied by the stratification (q_1); the second and third terms represent the horizontal (q_2) and vertical (q_3) shear vorticity including stratification. The the PV flux (PVF)

is defined as follows:

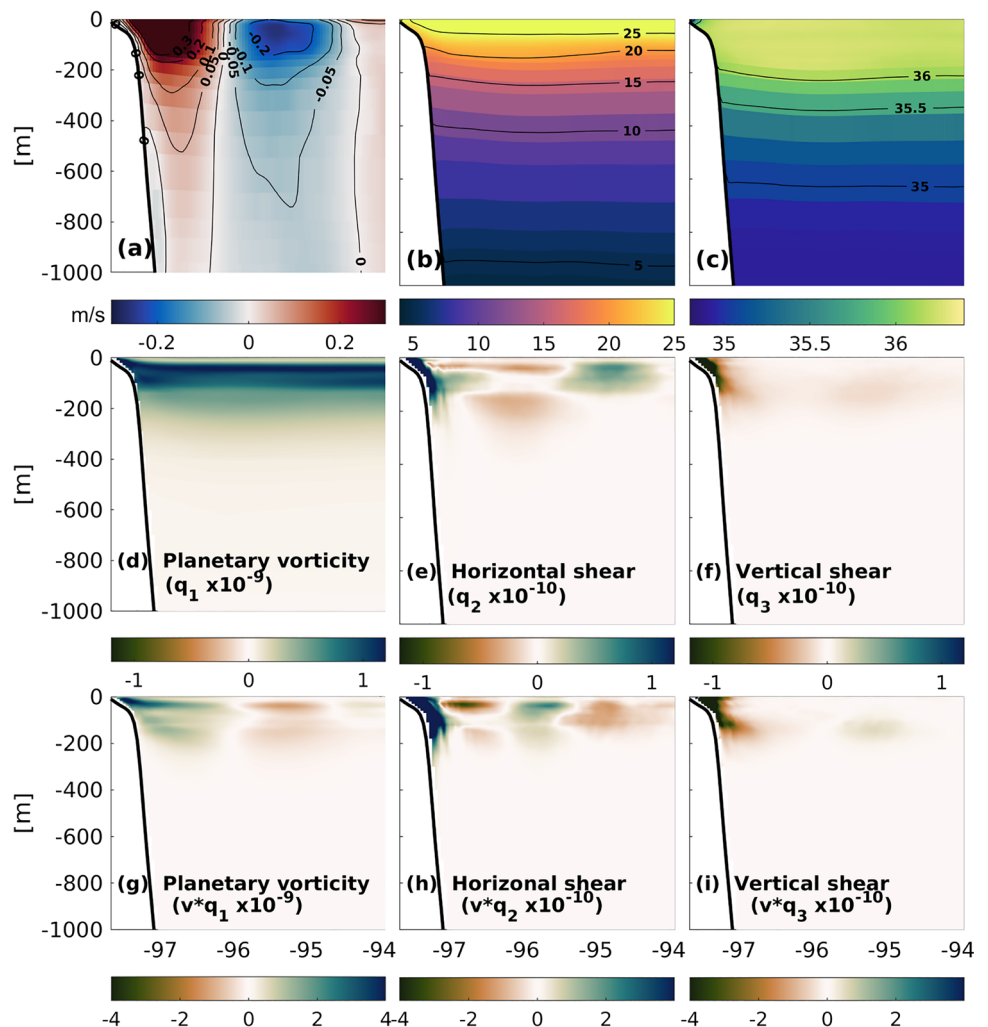
$$PVF = \iint vq dx dz \quad (4)$$

where the double integral is taken over the cross section from the bottom to the surface. The time integral of this flux, called “Cumulative PVF,”

$$CPVF = \int PVF dt \quad (5)$$

To estimate the PVF through the BoC and examine the behavior of the CG when LCEs collide with the southwestern boundary, we compute the PV terms on Eq. 3 in a zonal section at 22° N, between 97.6° W and 94.0° W (red dashed line in Fig. 8b) for the experiment OBW. The selection of this section was made considering the composite of SSH and surface velocity fields for periods when LCEs reached this region (Fig. 8b). Figure 12a–c show the 19-year mean vertical sections of meridional velocity, potential temperature, and salinity at 22°N respectively, with a zoom in the upper

Fig. 12 Mean quantities in a zonal section at 22° N (Fig. 5b) for experiment OBW: **a** meridional velocity, **b** temperature, **c** salinity, **d** planetary vorticity term q_1 ($\times 10^{-9} s^{-1} m^{-1}$), **e** relative vorticity horizontal shear q_2 ($\times 10^{-10} s^{-1} m^{-1}$), **f** relative vorticity vertical shear q_3 ($\times 10^{-10} s^{-1} m^{-1}$), **g** vq_1 ($\times 10^{-9} s^{-2}$), **h** vq_2 ($\times 10^{-10} s^{-2}$), and **i** vq_3 ($\times 10^{-10} s^{-2}$)



1000 m. The v -section shows two high speed current cores, one positive on the western part of the section and one negative to the east, surface-intensified but extending to 1000 m with weaker currents, representing a strong anticyclonic circulation on average. Temperature shows strong stratification throughout the section in the upper 1000 m and isothermals rising and outcropping above the western upper slope. The salinity contours show the characteristic subsurface salinity maximum at around 100 m represented by the subtropical underwater with salinity maximum ≈ 36.50 psu at $T \approx 23^\circ\text{C}$.

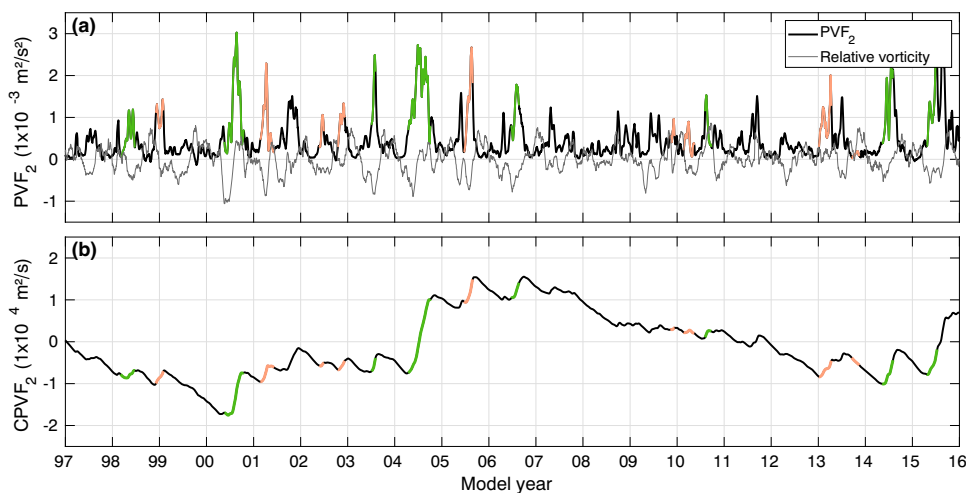
Sections d–f in Fig. 12 show the 19-year means of the three PV terms in Eq. 3: q_1 , q_2 , and q_3 . Of the three terms, q_1 is the largest, although it merely reflects the strong stratification near the surface. The q_1 depicts a region of strong positive shear near the surface on the western part of the section, related to the interaction of LCEs with the continental slope, and a secondary area of negative shear to the east, related to the center of the mean anticyclonic circulation in Fig. 12a. The q_3 has its largest values near the surface on the western portion of the channel but has small magnitudes compared to q_2 . In addition, mean sections of “ vq ” reflect the q values weighted by v (Fig. 12g–i). The mean vq_1 and vq_3 show large magnitudes near the surface but with opposite patterns and with vq_1 an order of magnitude larger. The mean vq_2 shows large magnitude on the western side of the channel, between the continental shelf and the northward current core of the eddy. It will become evident that most of the contribution to PVF2 is from those vq_2 -values.

The PVF due to q_1 is the largest, but we found that it is unrelated to the LCEs variability in the southwestern GoM; PVF due to q_3 is highly anti-correlated with the PVF due to q_2 but smaller in magnitude (not shown). Therefore, we only discuss the vorticity flux associated with the horizontal shear (PVF2), which is the component closely related with the presence of LCEs in the southwestern GoM. Figure 13 shows the time series of PVF2 (panel a) and CPFV2

(panel b), along with the integrated relative vorticity within the BoC (calculated within the box shown in Fig. 7b). PVF2 has been low-passed to remove signals shorter than 15 days; CPFV2 has been de-trended following Candela et al. (2002, 2003), which allow us to get a better view of the crests and troughs of the generally monotonic function CPFV2. The time periods when LCEs penetrated into the BoC are highlighted in orange and green according to our classification of the type of event. It is observed that in each of the 17 events, the presence of LCEs coincide with the peaks in the PVF2 curve, indicating a northward flux of positive vorticity with different magnitudes. In fact, the most prominent peaks in the time series occur during LCE penetration events. Using the same reasoning as Candela et al. (2002, 2003) and Oey et al. (2004), this can be interpreted as a northward flux of fluid parcels with strengthening cyclonic vorticity. We also see that PVF2 is entirely positive, a consequence of the dominant cyclonic shear on the western portion of the section (continental slope) near the surface and the strong northward velocities there, and that in the absence of LCEs, PVF2 is weaker.

In the behavior of CPFV2 (Fig. 13b), which is characterized by alternating periods of positive and negative fluxes lasting several months, it is evident the presence of LCEs. Over the 19-year simulation, virtually all the periods when LCEs penetrated into the BoC occurred during a period of cyclonic flux, or upward “trend,” of CPFV2 which in some cases are more extended than others (e.g., years 2000 and 2004). These results indicate that the northward flux of positive vorticity is driven by the strong positive shears weighted by the northward velocities of the western branch of a LCE. This also explains the results of the drifter analysis applied to three LCEs influencing the CG in Pérez-Brunius et al. (2013), in which water in the CG is displaced by the presence of the LCE, some of it entraining into the northward flow between the LCE and the continental shelf.

Fig. 13 **a** Time series of horizontal shear flux (integrated vq_2) through the zonal section at 22°N and **b** cumulative horizontal shear flux through 22°N . Time periods when the LCE influence the CG by decelerating it are highlighted in orange, and time periods when the cyclone accompanying the LCE entered the BoC and intensified the CG are highlighted in green. In **a**, relative vorticity integrated over the BoC (gray line) is also shown



To provide further insight into the influence of LCEs on the CG circulation, we incorporated the time evolution of the meridional velocity in the 22° N zonal section, the vq sections at 22° N, and the time series of PVF2 and CPFV2 in the movie of the supplemental material. From Fig. 13, it is observed that in our examples of the two types of LCE penetration events represented in the model years 2000 and 2001, the PV flux is high. Indeed, in both events, the peaks in PVF2 are related to strong southward penetration of the LCEs into the BoC. Nevertheless, it is important to mention that not all peaks in PVF2 are related to a deceleration and disruption of the CG. In the type of events corresponding to the year 2000, no organized cyclonic circulation is usually present before the arrival of the LCE, and it is only when its accompanying cyclone enters the BoC that the corresponding northward vorticity flux due to the LCE increases (Fig. 10g). On the other hand, in the type of events corresponding to the year 2001, the western BoC usually shows a well-formed, strong CG before the arrival of a LCE. Therefore, the deceleration or interruption of the CG can be explained by the increase in PVF2 out of the western BoC (Fig. 11g). These findings support the results proposed by both Pérez-Brunius et al. (2013), in which the presence of LCEs against the northwestern boundary of the BoC drains vorticity out of the CG, and by Vidal et al. (1992), in which the LCEs transfer mass and angular momentum into the BoC, strengthening the CG.

4 Summary and conclusions

In this study, we addressed the role that the large-scale, low-frequency winds and the LCEs reaching the northern BoC play in the mean, seasonal, and non-seasonal modulation of the CG by conducting a set of long-term free-running numerical simulations configured for the GoM using HYCOM, in which we turn on and off these two forcings. The multi-year nature of these experiments provided confidence about the statistical consistency of our results, since they were able to capture the regular (year by year) contribution of the wind stress to the BoC circulation and reproduce a long record of events when LCEs influenced the CG. According to experiment NoOBW, in the absence of LCEs, the wind can sustain a surface-intensified, nearly-symmetric cyclonic circulation in the western BoC, confined within the upper ~ 600 m. When the LC system is taken into consideration in experiment OBW, and thus the LCEs influence over the BoC, a cyclonic circulation is also present below ~ 1000 m, with mean velocities of $\sim 5 \text{ cm s}^{-1}$ throughout the water column. Our results indicate that this feature is merely the expression of the larger-scale cyclonic bottom boundary current.

According to OBNoW, in the absence of wind, the net effect of LCEs and their accompanying cyclones results in a weak cyclonic circulation in the upper layers of the west-

ern BoC (Fig. 5c) but with no surface signature. From our examination of the LCE influence on the western BoC circulation for experiment OBW, we conclude that this behavior in OBNoW can be attributed to the average contribution of the cyclones accompanying LCEs which eventually enter the BoC upon some events of LCE collision. The above also corroborates previous findings that the particular topography of the basin may be controlling the location of the CG.

To evaluate the role of topography for the three different experiments, we diagnosed the equivalent-barotropic nature of the flow within the CG. In all the cases, the equivalent depth resulted in closed geostrophic contours to the west of the BoC, confirming that topography plays a role in the position of the CG, regardless of the mechanism driving its variability.

The high, lagged correlation coefficients ($R > 0.8$, 5–15 days of lag) between the climatological transport in the western arm of the CG for OBW and NoOBW, and the seasonal component of the wind stress curl averaged over the BoC, provided evidence about the driver of the seasonal signal of the CG. One primary effect of LCEs is to impose high fluctuations on the circulation of the CG, contributing to its intraseasonal variability. When the LCEs present a significant southward penetration, these fluctuations lead to reversals in the transport, which occur when the northward currents of the western arm of the LCE replace the southward currents of the western arm of the CG, resulting in the interruption of the gyre from its unperturbed state. Conversely, when the LCE is accompanied by a large cyclone to its east, which eventually enters the BoC, it contributes to the CG intensification as had been previously proposed and hypothesized in previous studies (Vidal et al. 1992; Vázquez et al. 2005). Either of these two mechanisms is found to be consistent in all the events throughout the entire simulation. Finally, we found that the vorticity flux due to horizontal shear through the BoC becomes a good indicator of the influence of LCEs on the BoC circulation. The model results indicate that a northward flux of cyclonic vorticity out of the BoC occurs during most of the events of LCE southern penetration, resulting in the disruption of the CG.

Our results add evidence on the equivalent-barotropic nature of the CG in the absence of any forcing, with the wind stress curl and LCEs as the primary factors driving its variability and topography controlling its location. However, additional approaches to deepen the role of topography can be explored: one such alternative is to perform artificial modifications of the bathymetry over the BoC in such a way that potential vorticity contours f/F_0 are open instead of closed in a realistic model setup. In this way, the formation of the CG could be prevented, or its location could change. Such an analysis is proposed for future research. Although we identified some events in the three experiments, especially for OBW, further studies are needed to establish the mechanisms

and contribution of locally generated eddies to the variability of the CG and their importance in cross-shelf transport processes in the southern GoM.

Supplementary information This version of the article includes a movie as a supplementary material archived in the Zenodo repository <https://doi.org/10.5281/zenodo.6505406>

Acknowledgements This work is a contribution of Project 201441 funded by SENER-CONACyT through the CIGoM consortium. The first author thanks the program of postdoctoral fellowships UNAM-DGAPA, as well as the Instituto de Ciencias de la Atmósfera y Cambio Climático of the Universidad Nacional Autónoma de México for the use of the supercomputer Omoteotl to run the simulations. The authors thank the support of Pavel Oropeza in setting up the HPC environment for the execution of the simulations and Susana Higuera and Juan Nieblas for their help in processing the data for the validation of the model. We thank the editor, Dr. Ricardo de Camargo, and the two anonymous reviewers for their valuable contributions to the manuscript. Erick R. Olvera-Prado would like to acknowledge Eric Chassignet, Steve Morey, and Alex Bozec (Florida State University) for their advice, motivation, and guidance when conducting an equivalent set of simulations during his PhD studies.

Funding This study was funded by the program of postdoctoral fellowships UNAM DGAPA.

Data availability The datasets generated during and/or analyzed during the current study are not publicly available but may be available from the corresponding author on reasonable request.

Declarations

Conflict of interest The authors declare no competing interests.

Open Access This article is licensed under a Creative Commons Attribution 4.0 International License, which permits use, sharing, adaptation, distribution and reproduction in any medium or format, as long as you give appropriate credit to the original author(s) and the source, provide a link to the Creative Commons licence, and indicate if changes were made. The images or other third party material in this article are included in the article's Creative Commons licence, unless indicated otherwise in a credit line to the material. If material is not included in the article's Creative Commons licence and your intended use is not permitted by statutory regulation or exceeds the permitted use, you will need to obtain permission directly from the copyright holder. To view a copy of this licence, visit <http://creativecommons.org/licenses/by/4.0/>.


References

- Athié G, Sheinbaum J, Leben R et al (2015) Interannual variability in the Yucatan Channel flow. *Geophys Res Lett*, 42(5):1496–1503. <https://doi.org/10.1002/2014GL062674>
- Athie G, Sheinbaum J, Candela J et al (2020) Seasonal variability of the transport through the Yucatan Channel from observations. *J Phys Oceanogr*, 50:343–360
- Beal LM, Bryden HL (1999) The velocity and vorticity structure of the Agulhas Current at 32°S. *J Geophys Res Oceans*, 104(C3):5151–5176. <https://doi.org/10.1029/1998JC900056>
- Bleck R (2002) An oceanic general circulation model framed in hybrid isopycnic–Cartesian coordinates. *Ocean Model*, 4(1):55–88
- Candela J, Sheinbaum J, Ochoa J et al (2002) The potential vorticity flux through the Yucatan Channel and the Loop Current in the Gulf of Mexico. *Geophys Res Lett* 29(22):16–1–16–4. <https://doi.org/10.1029/2002GL015587>
- Candela J, Tanahara S, Crepon M et al (2003) Yucatan Channel flow: observations versus clipper ATL6 and MERCATOR PAM models. *J Geophys Res Oceans* 108(C12):15–1–15–24. <https://doi.org/10.1029/2003JC001961>
- Candela J, Ochoa-de-la Torre J, Sheinbaum J et al (2019) The flow through the Gulf of Mexico. *J Phys Oceanogr.* <https://doi.org/10.1175/JPO-D-18-0189.1>
- Vázquez de la Cerda AM, Reid RO, DiMarco SF et al (2005) Bay of Campeche circulation: an update. In: Sturges W, Lugo-Fernandez A (eds). *Circulation in the Gulf of Mexico: Observations and Models*. American Geophysical Union (AGU), p 279–293. <https://doi.org/10.1029/161GM20>
- Chassignet EP, Hurlburt HE, Smedstad OM et al (2006) Generalized vertical coordinates for eddy-resolving global and coastal ocean forecasts. *Oceanography* 19
- Dimarco SN Jr, Reid R (2005) A statistical description of the velocity fields from upper ocean drifters in the Gulf of Mexico. In *Circulation in the Gulf of Mexico: Observations and Models* (eds W. Sturges and A. Lugo-Fernandez). <https://doi.org/10.1029/161GM08>
- Donohue KA, Hamilton P, Leben R et al (2008) Survey of deepwater currents in the northwestern Gulf of Mexico, volume 2: Technical report. MMS Tech. Rep. MMS 2008-031, MMS
- Dukhovskoy DS, Leben RR, Chassignet EP et al (2015) Characterization of the uncertainty of loop current metrics using a multidecadal numerical simulation and altimeter observations. *Deep-Sea Res I*, 100:140–158. <https://doi.org/10.1016/j.dsr.2015.01.005>
- Furey H, Bower A, Perez-Brunius P et al (2018) Deep eddies in the Gulf of Mexico observed with floats. *J Phys Oceanogr* 48(11):2703–2719. <https://doi.org/10.1175/JPO-D-17-0245.1>
- Kundu PK (1976) Ekman veering observed near the ocean bottom. *J Phys Oceanogr*, 6(2):238–242
- Leben RR (2005) Altimeter-derived loop current metrics. Sturges W, Lugo-Fernandez A (eds). In: *Circulation in the Gulf of Mexico: observations and models*. American Geophysical Union (AGU), p 181–201
- Liu Y, San Liang X, Weisberg RH (2007) Rectification of the bias in the wavelet power spectrum. *J Atmos Ocean Technol*, 24(12):2093–2102. <https://doi.org/10.1175/2007JTECH0511.1>
- Metzger E, Helber R, Hogan P et al (2017) Global ocean forecast system 3.1 validation testing p 60
- Monreal-Gómez MA, Salas de León D, (1997) Circulación y estructura termohalina del golfo de México. *Contribución a la Oceanografía Física en México*. Monogr Unión Geofís Mex 3:1045–newpage1064
- Morey SL, Gopalakrishnan G, Pallás Sanz E et al (2020) Assessment of numerical simulations of deep circulation and variability in the Gulf of Mexico using recent observations. *J Phys Oceanogr*, 50:1045–1064. <https://doi.org/10.1175/JPO-D-19-0137.1>
- Oey LY (2004) Vorticity flux through the Yucatan Channel and Loop Current variability in the Gulf of Mexico. *J Geophys Res*, 109. <https://doi.org/10.1029/2004JC002400>
- Ohlmann JC, Niiler PP, Fox CA et al (2001) Eddy energy and shelf interactions in the Gulf of Mexico. *J Geophys Res Oceans*, 106(C2):2605–2620. <https://doi.org/10.1029/1999JC000162>
- Olvera-Prado ER, Moreles E, Zavala-Hidalgo J, Romero-Centeno R (2023) Upper-lower layer coupling of recurrent circulation patterns

- in the Gulf of Mexico. *J Phys Oceanogr*, 53:533–550. <https://doi.org/10.1175/JPO-D-21-0281.1>
- Pedlosky J (1987) Geophysical fluid dynamics. Springer, doi 10(1115/1):3157711
- Pérez-Brunius P, García-Carrillo P, Dubranna J, et al (2013) Direct observations of the upper layer circulation in the southern Gulf of Mexico. *Deep Sea Research Part II: Topical Studies in Oceanography, modern Physical Oceanography and Professor H.T. Rossby* 85:182–194. <https://doi.org/10.1016/j.dsr2.2012.07.020>
- Pérez-Brunius P, Furey H, Bower A et al (2018) Dominant circulation patterns of the deep Gulf of Mexico. *J Phys Oceanogr*, 48(3):511–529. <https://doi.org/10.1175/JPO-D-17-0140.1>
- Romanou A, Chassignet EP, Sturges W (2004) Gulf of Mexico circulation within a high-resolution numerical simulation of the North Atlantic Ocean. *J Geophys Res Oceans* 109(C1). <https://doi.org/10.1029/2003JC001770>
- Roussel C, Beal LM (2010) Observations of the Florida and Yucatan currents from a Caribbean cruise ship. *J Phys Oceanogr*, 40(7):1575–1581. <https://doi.org/10.1175/2010JPO4447.1>
- Saha S, Moorthi S, Pan HL et al (2010) The NCEP climate forecast system reanalysis. *Bull Am Meteorol Soc*, 91(8):1015–1058. <https://doi.org/10.1175/2010BAMS3001.1>
- Sheinbaum J, Candela J, Badan A et al (2002) Flow structure and transport in the Yucatan Channel. *Geophysical Research Letters* 29(3):10–1–10–4. <https://doi.org/10.1029/2001GL013990>
- Sturges W (1993) The annual cycle of the western boundary current in the Gulf of Mexico. *J Geophys Res Oceans* 98(C10):18,053–18,068. <https://doi.org/10.1029/93JC01730>
- Gutiérrez de Velasco G, Winant CD (1996) Seasonal patterns of wind stress and wind stress curl over the Gulf of Mexico. *J Geophys Res Oceans* 101(C8):18,127–18,140. [10.1029/96JC01442](https://doi.org/10.1029/96JC01442)
- Vidal VMV, Vidal FV, Pérez-Molero JM (1992) Collision of a loop current anticyclonic ring against the continental shelf slope of the western Gulf of Mexico. *J Geophys Res Oceans* 97(C2):2155–2172. <https://doi.org/10.1029/91JC00486>
- Vukovich FM (2007) Climatology of ocean features in the Gulf of Mexico using satellite remote sensing data. *J Phys Oceanogr*, 37(3):689–707. <https://doi.org/10.1175/JPO2989.1>
- Zavala-Hidalgo J, Morey SL, O'Brien JJ (2003) Seasonal circulation on the western shelf of the Gulf of Mexico using a high resolution numerical model. *J Geophys Res Oceans*, (1978-2012) 108(C12). <https://doi.org/10.1029/2003JC001879>
- Zavala Sansón L (2019) Nonlinear and time-dependent equivalent-barotropic flows. *J Fluid Mech*, 871:925–951. <https://doi.org/10.1017/jfm.2019.354>

Publisher's Note Springer Nature remains neutral with regard to jurisdictional claims in published maps and institutional affiliations.

Authors and Affiliations

Erick R. Olvera-Prado¹  · Rosario Romero-Centeno¹ · Jorge Zavala-Hidalgo¹ · Efraín Moreles² · Angel Ruiz-Angulo³

Rosario Romero-Centeno
rosario@atmosfera.unam.mx

Jorge Zavala-Hidalgo
jzavala@atmosfera.unam.mx

Efraín Moreles
moreles@cmarl.unam.mx

Angel Ruiz-Angulo
angel@hi.is

¹ Instituto de Ciencias de la Atmósfera y Cambio Climático, Universidad Nacional Autónoma de México, 04510 Mexico City, Coyoacan, Mexico

² Instituto de Ciencias del Mar y Limnología, Universidad Nacional Autónoma de México, 04510 Mexico City, Coyoacan, Mexico

³ Institute of Earth Sciences, University of Iceland, 102 Reykjavik, Iceland